Early steps of oxidative damage in DNA quadruplexes are position-dependent: quantum mechanical and molecular dynamics analysis of human telomeric sequence containing ionized Guanine.

Haritha Asha [a], Petr Stadlbauer [b], Lara Martínez-Fernández [c], Pavel Banáš [b,d], Jiří Šponer [b,*], Roberto Improta [a,*], Luciana Esposito [a,*]

[a] Istituto Biostrutture e Bioimmagini, Consiglio Nazionale delle Ricerche, Via Mezzocannone 16, 80136, Napoli, Italy

[b] Institute of Biophysics of the Czech Academy of Sciences, Královopolská 135, 612 65 Brno, Czech Republic

[c] Departamento de Quimica, Facultad de Ciencias and Institute for Advanced Research in Chemistry (IADCHEM), Universidad Autonoma de Madrid, Campus de Excelencia UAM-CSIC, 28049 Madrid, Spain

[d] Regional Centre of Advanced Technologies and Materials, Czech Advanced Technology and Research Institute, Palacký University, Křížkovského 8, 779 00 Olomouc, Czech Republic

Correspondence: sponer@ncbr.muni.cz, robimp@unina.it, luciana.esposito@cnr.it.

Abbreviations

$G^{\bullet+}$ (or simply G^{+}), Guanine radical cation; G4, G-quadruplex; MD, Molecular dynamics; QM, Quantum Mechanics; MM, Molecular Mechanics; Tel21, DNA sequence $GGG(TTAGGG)_3$; Tel22, DNA sequence $AGGG(TTAGGG)_3$; Tel21Gx^{+}, Tel21 sequence containing the xth G base as radical cation; LL1, lateral loop1 T4-T5-A6; LL2, lateral loop2 T16-T17-A18; DL, diagonal loop T10-T11-A12; PCM, Polarizable Continuum Model; PDB, Protein Data Bank; RMSD, root mean square deviation; RMSF, root mean square fluctuation; TR, time-resolved spectroscopy; G-H1, Guanine radical obtained by deprotonation at N1 atom; G-H2, Guanine radical obtained by deprotonation at N2 atom.

Keywords

Guanine quadruplex; Guanine radicals; electrostatic repulsion; solvation; DNA structure.

Abstract

Guanine radical cation ($G^{\bullet+}$) is a key intermediate in many oxidative processes occurring in nucleic acids. Here, by combining mixed Quantum Mechanical/Molecular Mechanics calculations and Molecular Dynamics (MD) simulations, we study how the structural behaviour of a tract $GGG(TTAGGG)_3$ (hereafter Tel21) of the human telomeric sequence, folded in an antiparallel quadruple helix, changes when one of the G bases is ionized to $G^{\bullet+}$ ($Tel21^+$). Once assessed that the electron-hole is localized on a single G, we perform MD simulations of twelve $Tel21^+$ systems, differing in the position of $G^{\bullet+}$ in the sequence. When $G^{\bullet+}$ is located in the tetrad adjacent to the diagonal loop, we observe substantial structural rearrangements, which can decrease the electrostatic repulsion with the inner Na^+ ions and increase the solvent exposed surface of $G^{\bullet+}$. Analysis of solvation patterns of $G^{\bullet+}$ provides new insights on the main reactions of $G^{\bullet+}$, i.e. the deprotonation at two different sites and hydration at the C8 atom, the first steps of the processes producing 8oxo-Guanine. We suggest the main structural determinants of the relative reactivity of each position and our conclusions, consistent with the available experimental trends, can help rationalizing the reactivity of other G-quadruplex topologies.

1. Introduction

Guanine-rich DNA and RNA sequences can adopt a non-canonical fold, a quadruple helix (G4), where four guanines (G) are arranged in stacked tetrads, stabilized by Hoogsteen hydrogen bonding network, and forming an inner channel containing metal cations (such as Na^+ or K^+), which are fundamental for their stability (**Fig. 1**).[1, 2] It is assessed that these structures can be present also in vivo[3] and there is an increasing awareness on their fundamental biological role since they have been implicated in a range of processes including transcriptional regulation, replication, genomic and epigenetic instability, telomere functioning, etc.[4-6] Given the importance of all these processes for the biology and the growth of cancer cells, G4s are becoming more and more promising molecular targets in cancer therapeutics.[7, 8]

G is the most readily oxidizable base[9] and its ionization energy is reduced by stacking,[10, 11] making G tracts even more susceptible to oxidation than isolated Gs. It is thus not surprising that G4s are particularly prone to oxidative damage, induced by the presence of oxidizing agents [12, 13] or by absorption of light.[14] Very recent experiments have shown that irradiation of DNA by UVC and UVB light can induce its oxidation without the presence of photosensitizers.[15, 16] This 'one photon' oxidative process is particularly affecting G4 molecules, which have the largest quantum yield (QY) among the different systems investigated (QY= 3∼6 x 10^{-3}),[17] comparable to the more frequently occurring photoinduced damaging reactions in DNA (e.g. pyrimidine dimerization). Moreover, this process produces a highly reactive radical species, G radical Cation, $G^{\bullet+}$ (simply denoted as G^+ throughout the paper). G^+ can undergo deprotonation both at N1 and N2 (**Fig. 2**) yielding radical species (G-H1 and G-H2, respectively).[13, 16, 18] Moreover, hydration of G^+ can lead to the formation of 8-oxoguanine (8-oxo-7,8-dihydroguanine, 8oxoG),[19] i.e. the most commonly encountered oxidative marker in DNA.[20] Interestingly, experiments show that G^+, G-H1 and G-H2 species can survive on the millisecond time-scale.[17] On the one hand, we thus have 'long-living' radical species that can trigger many other potentially dangerous photochemical events. On the other hand, the final photoproducts can lead to structural rearrangements of the G4s, undermining their biological functions. Fully understanding the molecular basis of oxidative damage in G4s is particularly important, and in this study, we try to make a step in this direction by performing a thorough computational study of the G4 formed by the human telomeric sequence repeat $GGG(TTAGGG)_3$, hereafter Tel21 (**Fig. 1**). Telomeres are G-rich sequences located, as for most of the eukaryotes, at the end of the chromosomes, playing a key role in many basic biological processes, from DNA replication, to ageing and apoptosis.[21-23]

By using Tel21 as a test system, we want to address some key questions concerning the structural basis of the formation and the reactivity of G^+ in G4. How does the formation of G^+ affect the structure of Tel21 and, conversely, how the G4 topology can dictate its preferential location? Do the observed geometry shifts depend on the position of G^+? How does the hydration of different Gs change upon ionization? We remind that the main reactive channels of G^+, i.e. deprotonation and hydration, critically depend on the presence of water molecules surrounding G^+. These general questions are potentially relevant also for possible use of G4 in nanotechnological applications,[24-26] a field of increasing interest, since G^+ is expected to be a key player in all the processes involving the transfer of an electron-hole.[12, 27] These issues will be tackled by integrating Quantum Mechanical calculations [16, 28-40] and Molecular Dynamics (MD) simulations, already extensively used to investigate G4 systems.[24, 41-48]

In detail, we resort to Quantum Mechanical (QM) /Molecular Mechanics (MM) calculations to study Tel21 and its 12 derivatives containing one G^+ ($Tel21^+$) at a different position. After having

ascertained that the cation is always almost perfectly localized on a single G base, we perform a thorough MD conformational analysis of Tel21, Tel22 (the sequence $AGGG(TTAGGG)_3$, for which an experimental NMR structure has been determined[49] and the twelve $Tel21^+$ sequences. In our study we focus mainly on the antiparallel basket topology typically adopted in the presence of Na^+ cations. Although the physiological concentration of Na^+ is smaller than that of K^+, in the presence of the former ion the structural variability is limited, with one topology largely dominant. Moreover, for $Tel21/Na^+$ accurate time-resolved experiments of ionized Tel21 are available.[17] This makes this system a very useful model for trying to unveil some general structural trends induced by G ionization. Additionally, in order to get specific insights on the roles played by the folding topology and the inner cation, we also studied some key positions of Tel21 sequence adopting the hybrid-1 topology [50] in the presence of K^+ (see SI for details). Our study shows that the presence of a G^+ base always causes some local perturbations of the Tel21 structure and, for some positions, major structural distortions of the quadruplex structure are observed. We predict that tetrad1 (see **Fig. 1**), the one closest to the diagonal loop (DL), is perturbed by the presence of a G^+ the most, especially when it is in position 1, 13, and 21 (**Fig. 1**). The comparison between the conformational behavior of Tel21/Tel22 and $Tel21^+$ provides insights on the driving forces affecting the structural properties of a sequence containing a G^+, such as, for example, the tendency to increase the solvent exposure of G^+ and its distance from the inner cations. On this ground, our study gives useful and general indications on the positions more prone to formation of G^+ or to its migration following ionization of another base. The results are relevant not only for Tel21 but also for other sequences and G4 folding topologies. Finally, based on the analysis of the behavior of the different $Tel21^+$ species, the most important factors (e.g. the local structural flexibility, the proximity with the inner Na^+ ions or the interaction with the solvent) affecting the reactivity of the different positions with respect to the oxidative damage are critically discussed in the framework of the available experimental data. [51]

2. Material and Methods

2.1. QM/MM computational details

To model the Tel21 sequence $d(G_3(TTAG_3)_3)$ we started from the basket-type antiparallel G4 structure determined by NMR in solution in presence of Na^+ ions for the Tel22 sequence (PDB ID 143D, model 1 [49]), which differs from Tel21 by an additional adenine (A) at the 5'-end (**Fig. 1**). The Electronic Circular Dichroism spectra of $Tel21/Na^+$ and $Tel22/Na^+$ are almost superimposable, which strongly indicates that $Tel21/Na^+$ also adopts the basket-type antiparallel topology.[52-54] The 5'-A truncated Tel22 structure with two manually added Na^+ ions in the inter-tetrad space (see Section 3.1 below for details), was used as starting geometry for our QM/MM geometry optimizations. The QM region includes all the G bases in the G4 core, the closest bases of the loops (T5, A6, A12, A18, **Fig. S1A**) and the inner Na^+ ions. Density functional theory (DFT), with the M052X[55] functional combined with the 6-31G(d) basis set was used for the description of this region. The rest of the nucleobases in the loop, the backbone and outer Na^+ ions were computed at the MM level (amber force field parm96.dat).[56] Both the regions were coupled using the ONIOM interface.[57] The whole QM/MM system was embedded in implicit water using a Polarizable Continuum Model (PCM).[58, 59] This procedure has been successfully applied to previous theoretical studies involving G4,[16, 29-32] giving absorption spectra for neutral and radical species in good agreement with

experimental results. After Tel21/Na^+ ground state optimization, we have optimized 12 different cationic species, in which the G radical cation was located at the different positions of the G4. All the QM/MM calculations were performed by using Gaussian package.[60]

2.2. MD simulation details

Models

Our MD simulations used the same starting structure as the QM/MM calculations. When comparing Tel21 and Tel22 sequences, we numbered the 5'-A in Tel22 as A0 in order to keep the same base numbering. Two Na^+ ions, not present in the experimental structure used, have been added inside the channel based on the positions they occupy in the deposited structure of the complex of Tel21 with a ruthenium ligand (PDB ID 2MCO).[61]

In the 143D G4 structure, the planar arrays of four Gs, held together by eight Hoogsteen hydrogen bonds (h-bonds), are denoted as tetrad1 (composed of G1, G9, G13, G21), tetrad2 (composed of G2, G8, G14, G20), and tetrad3 (composed of G3, G7, G15, G19). In this topology there are two lateral loops, LL, (loop1 denoted as LL1: T4-T5-A6; loop2 denoted as LL2: T16-T17-A18) and one diagonal loop (denoted as DL: T10-T11-A12) (**Fig. 1**).

We ran a set of 1 μs simulations for the neutral systems (Tel21 and Tel22 sequence) as well as for the 12 cationic systems (Tel21Gx^+, x = guanine number along the sequence), each of which contained a different G replaced by G^+. A list of all simulations is in **Table S1**.

Model 1 of the 143D structure was used as a starting structure for five out of ten simulations for the neutral system Tel21 (Tel21, Tel21_1, Tel21_2, Tel21_6, Tel21_7) and model 6 was used for four simulations (Tel21_3, Tel21_4, Tel21_8, Tel21_9). One simulation was initiated based on the structure most similar to the average structure in the simulations of Tel21G14+ (Tel21_5; **Table S1**). When reporting the results for the neutral systems, we shall refer to the averages calculated over the ten independent trajectories unless otherwise stated.

The cationic systems were prepared by starting from model 1 of the 143D structure and replacing one G by G^+, whose parameters have been developed as described below. We have run a second simulation for the cationic systems in the outer tetrads (i.e. tetrad1 and tetrad3), where larger distortions with respect to the starting structure are observed (denoted as Tel21Gx^+_2, x= 1,3,7,9,13,15,19,21). When reporting the results for these systems, we shall refer to the averages on the two simulations.

With the aim to check our results on a different topology with K^+ as inner cation, we also studied the effect of G^+ on the Tel21 sequence adopting the hybrid-1 G4 structure (PDB ID 2GKU, model 1, [50]) (**Fig. S1B**). In this hybrid-1 G4 structure (Tel21K) the tetrads are composed of the following G bases: tetrad1 (G1, G7, G15, G19), tetrad2 (G2, G8, G14, G20), and tetrad3 (G3, G9, G13, G21) (**Fig. S1B**). We carried out a set of four simulations for the neutral system (Tel21K simulations) as well as a set of two simulations for three cationic systems (Tel21KGx^+, x =7,8,9) (**Table S1**).

MD simulation settings

Classical MD simulations have been performed by using the Amber16 package[62] and the OL15 DNA force field.[63, 64] The parametrization of G^+ consisted of a charge density redistribution involving nucleobase atoms, on the ground of the RESP charges[65] computed at the DFT (PW6B95/def2-TZVP) level (see SI for more details). The parameters are given in the SI (**Table S2**). We expect that the main structural effect of G ionization would be essentially electrostatic, related

to the creation of an additional positive charge in the inner part of Tel21, and that can be captured by a classical force field.
The G4 models were immersed in a truncated octahedral water box with 10 Å solvation shell around the structure. Sodium and potassium ions were added to 143D and 2GKU models, respectively, achieve electroneutrality. Some water molecules were then replaced with Na^+ or K^+ and Cl^- ions to set an ionic strength of approximately 150mM excess salt (equivalent to 10 Na^+ or 10 K^+ and 10 Cl^- ions). The systems were solvated in the SPC/E water model[66] and the parameters for Na^+, K^+ and Cl^- are the SPC/E-adapted Joung and Cheatham parameters [67]; the used combination of force-field parameters have been extensively tested for G4 structures.[68]
MD simulations were carried out in periodic boundary conditions; electrostatic interactions were treated using the particle mesh Ewald method with a real space cutoff of 9 Å.[69] Lennard-Jones interactions were truncated at 9 Å. Berendsen weak coupling thermostat and barostat were used to maintain constant temperature and pressure of 300 K and 1 atm, respectively. All the systems were equilibrated using standard protocols previously described.[42] In the final production runs, the frames were written to the trajectory every 5 ps, resulting in 200000 structures to be analyzed for each 1 μs trajectory.

Trajectory analyses
The trajectories were visually inspected in VMD (version 1.9.3),[70] which was used to prepare figures together with PyMol (version 1.8.2.0).[71] The analysis of the trajectories was performed using the cpptraj module of Amber16.[72] The h-bond routine to calculate the occurrence of the interactions was applied by using the following cutoffs for donor (D)-acceptor (A) distance and angle: d_{AD}<3.3 Å, angle DH···A >135°. It is worth noting that any distance/angle cutoff is arbitrary, nonetheless, we use it for qualitative detection of simulation parts where the h-bonding interactions are less efficient/strong.
The planarity of the tetrads as well as their automatic identification in the individual structures along the trajectory was calculated by the G4 module in 3DNA-DSSR [73, 74]. For this analysis, 2000 structures were sorted out in each trajectory by sampling every 500 ps.
In specific cases, to have a more quantitative measure of the geometric distortion of a tetrad (see Tel21G9$^+$ tetrad1 planarity, in section 3.3.1), we calculated the best-fit tetrad plane through the ring atoms of the four Gs and then we analyzed the angle between the norm of each base and the norm of the best-fit tetrad plane (out-of-plane deviation angle for each base of the tetrad).
We computed the solvent accessible surface area (SASA) for all the studied systems, a parameter that has been adopted in the past to analyse the interaction between ions and DNA.[75, 76] We included both the DNA quadruplex and the two channel Na^+ and K^+ ions in the calculation. We used a standard GROMACS utility,[77] which implements the double cube lattice method with a probe radius of 1.4 Å. By this tool, we could extract the average values of SASA for the subset G ring atoms (including exocyclic atoms) from the total SASA area. These calculations were carried out on each trajectory sampled every 20 ps.
The analysis of the interactions of N1(H1), N2(H22), and C8(H8) groups with solvent were carried out using cpptraj on a trajectory sampled every 50 ps. We monitored direct hydrogen bonds as well as all proximal waters, which can interact with the base or make the deprotonation reactions easier. In this context, the thresholds for our selection was set at a distance between the water oxygen atom (O_w) and the base atom (D=N1, N2, C8) < 3.9 Å, and an angle O_w···H-D >90°. For each base and for each type of interaction (O_w-D), we considered the number of frames of the trajectories where

there is at least one water contact and analysed the averaged values of the O_w-D distances. We also took into account the average number of interactions between the group and the solvent per frame (hereafter denoted as fract_wat).

3. Results

3.1. Tel21/Na^+ and Tel21$^+$/Na^+: QM/MM results

We have optimized the geometry of Tel21 and Tel21$^+$ at the PCM/M052X/AMBER level, succeeding to locate the minimum for all possible locations of the electron hole. We have thus obtained 12 Tel21$^+$ minima, differing for the location of the G^+ base in the sequence (**Table S3**). Actually, this analysis has the first important goal of verifying the possibility that the electron hole is partially delocalized over more than one base.[31] In this respect, our calculations indicate that, for all the bases, the hole is essentially localized on a single G^+, which adopts the geometry very close to that of an isolated G^+ base.

The QM/MM calculations do not include the effect of thermal fluctuations of Tel21$^+$ and therefore do not provide insights into possible global conformational rearrangements of G4, since each geometry optimization simply converges to the first stable local minimum close to that optimized for the Tel21, as all systems share the same starting structure. On the other hand, the comparison between the minima of Tel21$^+$ and Tel21 highlights some interesting local effects. The presence of a G^+ base is mirrored by a shift of the inner Na^+ ions, which increase their distance from the cationic base, due to the onset of electrostatic repulsion. Moreover, a well-defined trend in the h-bond lengths of G^+ is observed (see **Table S3**). The h-bond lengths in which G^+ acts as a donor (i.e. N1-H1$\cdots$O6 and N2-H21$\cdots$N7, **Fig. 2**) become ~10-15% shorter, suggesting an increase of the h-bonding strength. In contrast, h-bonds involving G^+ as an acceptor are elongated to a similar extent. These shifts are fully consistent with the well-known increase of the acidity of H1 and H21 protons upon ionization of G. At the same time, our calculations indicate that the presence of G^+ breaks down the symmetric arrangement of a tetrad, with two pairs interacting more strongly. One formed by G^+ and the G base accepting its h-bonds, the other by the two remaining G bases. More details are given in the SI. To see such profound local rearrangements in QM/MM optimizations indicates that larger structural effects should be expected when allowing thermal sampling.

The presence of G^+ can affect also the coordination energy of the Na^+ ions, which are fundamental to stabilize G4. The study of the ion coordination to DNA by means of computational approaches is a very active research field, (see for example [36-38, 75, 76, 78, 79]) and exhaustive review of the different contributions is beyond the scope of this work. In our case, the G^+ is well buried in the quadruple helix and its effect is expected to be larger for the inner Na^+ ions (depicted in black in Fig. 1), which are closer to G^+ and not shielded by the phosphate groups and the solvent. Our test QM/MM calculations (see **Table S4**) show that G ionization leads to a decrease of the coordination energy of one inner Na^+ ion by ca 3 kcal/mol. The 'outer' Na^+ counter-ions are pretty distant from the G^+ (> 9 Å) and, indeed, our calculations show the interaction energy is almost unaffected by G ionization (< 0.5 kcal/mol, i.e. well below the expected accuracy of our estimates).

3.2. Conformational behaviour of Tel21/Na^+ and Tel22/Na^+: MD simulations

Simulations of undamaged Tel21 and Tel22 provide a reference for subsequent simulations analysing the effect of G^+ bases. As illustrated in detail in the SI, the conformational behaviour of Tel22 and Tel21 (loop flexibility, tetrad stability, h-bonding interactions, ion positions, etc.; **Figs. S2-S6, Tables S5-S10**) is fully consistent to that described in a previous study of Tel22/Na^+.[42] The antiparallel basket-type fold proves to be quite robust also in the absence of the 5'-terminal A as in Tel21. The three tetrads are well maintained during the simulations (**Figs. S2,S4,S6**, **Table S5**), so that the departures from the starting NMR structure mainly involve the rearrangement of loops (**Figs. S3-S4**), which are known to be flexible [38] and are not the goal of this work.

The stiffness of the tetrad arrangement is assessed by analysing the h-bonding pattern. Both the inner and the outer Hoogsteen patterns are fairly stable (**Table S5**). In particular, the outer pattern (in green in **Fig. 2**), involving N7···N2(H) atoms is strongly conserved during the simulations. The inner h-bonds involving O6···N1(H) atoms are less frequent (in yellow in **Fig. 2**).

Among the tetrads, tetrad3 is the stiffest, as well as the most planar (**Table S6**). Although tetrad3 is an outer tetrad, both the frequent interactions between LL1 and LL2 via Watson-Crick A:T base pairing (**Fig. 3A, Table S7**) and the stacking/h-bonding interactions between LL bases and Gs contribute to the stability of tetrad3 (**Fig. 3A, Table S7**) and its shielding from the solvent (**Table S9**). On the other hand, tetrad1 is the most flexible, showing the largest deviation from planarity, as well as containing the bases most exposed to solvent.

The only minor differences between Tel21 and Tel22 simulations involve both the dominant conformation of the DL (**Table S8, Fig. S5)** and the solvent exposure of tetrad1 bases (**Table S9)** due to the dynamics of both the DL and the flanking A0 base in Tel22. For instance, G13 and G1 bases are less solvent exposed in Tel22, due to both the presence of the A0 base and the G1 backbone phosphate which partially cover the rings (**Fig. S5**). Two main conformations are more common for the DL. One (denoted as *conformation1* and prevailing in Tel22) is characterized by extensive stacking of T10/T11/A12/G13 (**Fig. 3C, Table S8**) and was also previously found among the different conformations sampled by DL in the benchmark simulations on TTA loops of human telomeric G4s [42] (see also SI for details). The other (denoted as *conformation2* and prevailing in Tel21) is characterized by stacking of T11/G1 at the 5'-end and of A12/G21 at the 3'-end (**Fig. 3B**). DL *conformation2* seems to decrease the exposure of G1 (stacking with T11), G21 (stacking with A12) and G13 (the backbone between T11 and A12 stacks over G13).

Finally, according to our simulations, Na^+ ions residing inside the G4 channel are not equidistant from adjacent tetrads, but they are closer to the oxygen atoms (carbonyl O6) belonging to the outer tetrads, i.e. to tetrad1 and tetrad3 (**Table S10**). This arrangement allows minimizing the mutual electrostatic repulsion between the two Na^+ ions. This behaviour is consistent with that found by previous studies showing that small and mobile Na^+ can adopt a variety of positions inside the GQ ionic channel,[80-83] including coplanarity with the G bases.[84]

Additional details on the features of the neutral systems can be found in the SI and are compared with trends evidenced for Tel21$^+$ in the next sections.

3.3. Conformational behaviour of Tel21$^+$/Na^+ cationic systems: MD simulations

As a next step, we simulated different cationic systems of Tel21, where a single G was replaced by G^+, exploring all the 12 possible positions. As shown by the analysis of the root mean square deviations (RMSDs) with respect to the NMR starting structure, as well as by the root mean square fluctuations (RMSFs) of the bases, Tel21$^+$ remains folded over the course of the simulations **(Figs.**

S7-S9). However, we always observe some structural differences with respect to the undamaged sequence and the extent of the structural distortion induced by the presence of a G^+ in Tel21 dramatically depends on its position in the sequence. A full detailed report of tetrad properties, loop flexibility, ion and solvent interactions is given in the SI (**Tables S11-S24, Fig. S10**). Representative structures for the twelve cationic structures are shown in **Fig. 4** and **Figs. S11-S14**.

As can be seen, when G^+ is located in **Tetrad2**, we never observe significant structural shifts compared to neutral Tel21. As reported in detail in the SI, in this case, G^+ leads to some distortion of the h-bond pattern of tetrad2 (**Table S11**) and to a modest increase of the average distance between G^+ and the inner Na^+ ions (**Table 1**, **Table S12**).

Tetrad3 is more sensitive to the presence of G^+ than tetrad2. Indeed, in specific positions the h-bonding network is more perturbed (**Table S11**) and the increase of the G^+/Na^+2 ion distance is generally larger (**Table 1 and Table S12**). Interestingly, the distance between O6 and Na^+2 increases by 20% for $G19^+$, by 24% for $G15^+$, by 38% for G3 and by 44% for $G7^+$ with respect to Tel21 (**Table 1)**. The large increase found for $G3^+$ and $G7^+$ mirrors a significant distortion of tetrad3. $G7^+$ moves away from the centre of the array and from G19 (**Fig. S12**), consequently, tetrad3 is lost in 5% of structures along the Tel21$G7^+$ trajectories (**Table S13**). In the two simulations of $G3^+$, the charged base can either simply tilt out of tetrad3 plane, thus distorting planarity (0.57 Å in Tel21$G3^+$_2 vs. 0.36 in Tel21), or shift away from the centre of tetrad3, thus breaking the tetrad arrangement (in Tel21$G3^+$, tetrad3 is detected in only 53% of simulation time) (**Fig. S12**).

Finally, **Tetrad1** is affected by the presence of a G^+ the most. In one case ($G9^+$) we observe a strong alteration of the 'outer' h-bonding pattern. In the other three systems (Tel21 with $G13^+$, $G1^+$, $G21^+$) G^+ leads to disruption of the tetrad (**Table S11**) and swinging out of one or two bases. (**Fig. 4**).

In general, the behaviour of the LLs is not significantly different with respect to the neutral systems (**Fig. S8**, **Table S14**) whereas that of the diagonal one shows some differences, which we will discuss together with tetrad1.

In the next subsection, we give more details about the structural behaviour of the $Tel21^+$ systems where G^+ is located in tetrad1, i.e. those showing the largest distortion with respect to the undamaged system, while the analysis of the changes in the solvation patterns due to G^+ is reported in section 3.3.2.

3.3.1. Tetrad1

***G1*$^+$ cation.** In Tel21$G1^+$ simulation, a first conformational rearrangement takes place within the first 125 ns (**Fig. 5A**). After ~25 ns, $G1^+$ moves slightly away from its h-bonding partners G13 and G9, destabilizing the $G1^+$:G13 pair and breaking the regular arrangement of the tetrad. At this stage of the simulation, the distance between $G1^+$ O6 atom and Na^+1 increases from 2.3 Å up to 7 Å. A new stable rearrangement is then reached when $G1^+$ moves a little closer to centre of the channel. The outer h-bonds (N7···N2) are frequently broken, the most persistent one being that in the G9:G21 pair (**Table S11)**. Inner h-bonds (O6···N1) also rearrange, mainly due to a shift of the $G1^+$:G13 pair with respect to G9:G21 pair, leading to the establishing of N1···N7 h-bonds between G1:G9 and G13:G21, and consequent lower occurrence of N1···O6 h-bonds (**Table S11)**. Similar distortions in the h-bonding patterns are observed in the other independent simulation, Tel21$G1^+$_2 (**Table S11**). Consequently, in both simulations tetrad1 is not detected in ~20% of sampled trajectory structures (**Table S13**).

In Tel21G1$^+$ simulation, a more dramatic conformational rearrangement is observed after ~900 ns (**Fig. 5A** and **Fig. 6A**), so that the simulation was extended to 2 μs. At about 950 ns, G13 swings out of the tetrad plane breaking all its h-bonds to G1$^+$ and G21 and leaving a G-triad with regular Hoogsteen h-bonds (in the range 950-1800 ns, <RMSD$_{tetrad1}$>= 2 Å) (**Fig. 5A** and **Fig. 6A**). G13 lays above the plane, partially stacked over G1$^+$. In the latest 200 ns of the trajectory, the G13 base moved farther away from the core, becoming exposed to solvent (**Fig. S13**) as the triad is disrupted (<RMSD$_{tetrad1}$>= 4 Å) (**Fig. 5A**). Due to all these events, tetrad1 is present only in 13% of structures in the range 25-125 ns, in 98% of structures in the range 125-925ns and is never detected in the last μs of simulation (see also **Table S13**).

G9$^+$ cation. Among the simulations with a cation in tetrad1, Tel21G9$^+$ and Tel21G9$^+$_2 (**Fig. 5C** and **D**) show the least distorted structures. Nonetheless, both of them have higher and more dispersed RMSD values for tetrad1 compared to the neutral simulations (**Fig. S6**) (<RMSD$_{tetrad1}$>$_{2simu.}$=0.82 Å, <s.d.>$_{2simu.}$=0.18 Å *vs* <RMSD$_{tetrad1}$>$_{10simu.}$=0.69 Å, <s.d.>$_{10simu.}$=0.10 Å). The outer h-bond pattern is less regular than in Tel21 (**Tables S11, S5**). In particular, the h-bonding in G1:G9$^+$ is weakened (on average, less than one interbase h-bond occurs), hence two more stable pairs, G1:G13 and G9$^+$:G21, are formed. The weakening of the G1:G9$^+$ pair is mirrored by either G9$^+$ or G1 moving/tilting out of the tetrad1 plane (**Fig. 6B** and **Fig. 4A**), with a consequent increase of the corresponding distance from Na$^+$1. In all the Tel21 systems studied, the G9 base is strongly tilted out of the tetrad1 plane. Here in Tel21G9$^+$ the G9$^+$ ring is inclined at an angle of about 30 degrees (**Fig. 6B**). Due to the distortion induced by G9$^+$ the presence of tetrad1 is detected in only the 69% of structures (**Table S13**).

G13$^+$ cation. In both Tel21G13$^+$ and Tel21G13$^+$_2 simulations, in the first 10 ns of the simulation G13$^+$ moves away from the other three bases of tetrad1, rearranging its h-bonds with them. On the same time scale, G13$^+$ moves out of the tetrad plane and inserts itself between the DL loop and the triad G1-G9-G21 (**Fig. 4A**). In this new arrangement, G13$^+$ is packed between the ribose of A12 and G1 is thus shielded from the solvent (**Table 2, Table S16, Fig. S10**). The G13$^+$ position is stabilized by a direct interaction between the amino group of G13$^+$ and the phosphate oxygens of T11. Along the simulations, while G1 and G9 still keep some loose h-bonding pairing (**Table S11**), G21 moves outward, i.e. away from G1:G9 pair and from the centre of the original tetrad1 (**Fig. 6C**), and, in Tel21G13$^+$_2, becomes fully exposed to the solvent. These distortions are mirrored by the high RMSD of tetrad1 with respect to the starting structure (**Fig. 5E** and **F**) and attested by 3DNA-DSSR, which never detects tetrad1 in Tel21G13$^+$ (**Table S13**).

The electrostatic repulsion between G13$^+$ and Na$^+$1 appears as an important driving force of the conformational rearrangement. G13$^+$ moves out of the tetrad plane away from Na$^+$1 and their average distance increases (5.8 Å) (**Table 1 and Table S12**). The same occurs to G21 (average distance 6.9 Å, **Table S12**). Due to these structural shifts, Na$^+$1 gets closer to tetrad2 plane and, consequently, Na$^+$2 becomes almost coplanar to tetrad3 (**Fig. 6C**), occasionally moving out of the inter-tetrad region (**Fig. S14A**) towards the LL. Further details are provided in the SI.

G21$^+$ cation. In both simulations tetrad1 is disrupted within 10 ns (**Fig. 5G** and **H**) and it is detected only in 7% of the trajectory structures (**Table S13**). G21$^+$ moves out of the tetrad core and is no more stacked to G20 (**Fig. 6D**). G21$^+$ remains h-bonded with G13, but new h-bonds are formed between G13:G9 and G9:G1 (see **Fig. 6D** and SI for details). This global rearrangement leads to the formation of a triad composed of G1, G9, G13, with G13 stacked over G20. (**Fig. 6D** and **Fig. 4A**). Although being far from the triad, G21$^+$ establishes a new h-bond with G9 (O6···N2), present in 70% of structures (**Fig. 6D**). The new scheme of h-bonds reported in **Fig. 6D** holds for both simulations, but

in the last part of the Tel21G21$^+$_2 trajectory (from 850 ns onward), the G21$^+$ base breaks all connections to tetrad1 and becomes solvent exposed.
As in Tel21G13$^+$, these shifts are accompanied by a large increase of the distance between G21$^+$ and Na$^+$1 (**Table 1**). After less than 10 ns, G21$^+$ and G13 no longer interact with Na$^+$1, which then approaches tetrad2 (the average distance between Na$^+$1 and tetrad2 bases is 2.4~2.6 Å) (**Table S12**). Na$^+$2 stays close to tetrad3, but sometimes moves out of the tetrad2/tetrad3 space towards the LL (**Fig. S14B).**

3.3.2. Solvent exposure of Tel21$^+$

Next, we have examined the solvation patterns of Tel21$^+$. When the base is charged, we observe that its solvent accessible area (for the nucleobase and the whole nucleotide) generally increases compared to the neutral system (**Table 2, Fig. S10, Table S15-S16**). For three bases (G2, G9, and G20) the SASA values in Tel21 and Tel21$^+$ are lower or comparable, and only for G13 there is a remarkable decrease of solvent exposure once charged (**Fig. S10**), simply due to the insertion of G13$^+$ between the DL loop and the triad G1-G9-G21 (**Fig. 6C**), described above.
As anticipated, the conformation adopted by DL (T10-T11-A12) also affects the solvent accessibility of tetrad1. For example, when the DL is in *conformation 1* or *4* (with an extensive stacking involving loop bases and a tetrad G, see **Table S8**), the 5'-end G1 and G9 are more solvent exposed (**Tables S9, S16**). Also, G13 shows larger solvent exposure, despite its frequent stacking to A12, when DL is in *conformation 1* (**Tables S9, S16**). On the other hand, for G21 the *conformation2* of DL, with the stacking A12/G21, seems to restrict the exposure of G21 (**Tables S9, S16**).
We then focus more specifically on the interactions between the solvent and the N1(H), N2(H2), and C8(H) groups, those critical for the reactivity of G$^+$, since the radical cation can evolve through the deprotonation of the amino or imino groups or the hydration of C8.
The **N1-H1 group** is engaged in the inner h-bond pattern of the G-tetrad, hence it is the least accessible by water molecules, especially in the middle tetrad (tetrad2) (**Table S17**), even when G$^+$ is located there. The most accessible N1-H1 group in Tel21 is that of G7, whose interaction with water increases upon its ionization. Other N1-H1 groups showing some interactions with waters in the neutral state are G1, G13 and G9, with G1 having rather remarkably different behaviour dependent on the DL conformation. All of these bases, once charged, interact more frequently with waters, which is also observed for G3$^+$ and G21$^+$. In addition, the average distance between N1 of the charged base and water oxygen (solute-solvent distance) decreases (**Table S18**) to h-bonding interaction values (<3.3 Å). Therefore, these groups are potential candidates for the loss of proton from the radical cation.
For what concerns the amino **N2-H21-H22 group,** we focused on the interaction with waters of the **N2-H22** bond, which is not involved in the outer h-bonds of the tetrad (**Fig. 2**), and therefore is more accessible to solvent, even in the inner tetrad2, with the only exception of G3 and G19 (**Tables S19, S20**). Comparison with Tel21 simulation does not show any systematic increase of the number of interactions with the water molecules for G$^+$ (**Tables S19, S20**), but a significant decrease of the average **N2-H22**/water distance (**Fig. 7A**, **Table S21**). Upon G ionization, it is thus more probable that the water molecules around the N2-H22 form hydrogen bonds. For the only two positions where this trend is not observed (G19$^+$ and G21$^+$ in **Fig. 7A**) the N2-H22 of G$^+$ is h-bonded with its own phosphate.

The **C8-H8 group** is rather exposed to solvent also in Tel21 and its interaction with water is stronger for G^+. The number of frames of the trajectory with at least one water contact with C8-H8 (**Fig. 7B, Table S22**) increases; the water molecules are on average closer to the C8 atom (**Fig. 7C**, **Table S23**); the average number of water molecules around C8-H8 group per frame (**Fig. 7D**, **Table S24**) is larger. The positions for which the enhancement due to G^+ is more significant are **$G21^+$** (whose C8-H8 group is already well exposed in the neutral system) and, to a lesser extent, **$G9^+$** and **$G7^+$**.

3.4. Conformational behaviour of Tel21/K^+ and three cationic derivatives: MD simulations

Recent studies show that in K^+ solution Tel21 undergoes one photon ionization, and the resulting G^+ bases can survive on the ms time-scale.[85] In the presence of K^+, telomeric sequences are known to be polymorphic, mainly adopting two hybrid folding topologies, usually labelled hybrid-1 and hybrid-2, [42, 86] whose equilibrium is modulated by the nature/length of the flanking bases. Since several folds are probably accessible to Tel21/K^+ sequence, a full experimental/computational study on Tel21/K^+ conformational behaviour falls outside the scope of this study. However, in order to get preliminary insights on the effect of the folding topology and of the coordinated ion on the structural behaviour of $Tel21^+$, we compared the structural dynamics of neutral Tel21/K^+ with those of three systems, where one G^+ is at position 7, 8, or 9 (**Fig. S1B**). We choose these positions because they exhibit a very different reactivity with respect to oxidative reactions caused by one electron oxidants. Moreover, the reactivity of these positions is not dramatically affected by the adopted fold (hybrid-1 or hybrid-2).[51] As detailed in the SI, these calculations confirm the trends we evidenced for the basket topology. The presence of G^+ significantly affects the structural dynamics of hybrid-1 $Tel21^+$/K^+ (for the cations we have examined), as mirrored by the differences of several parameters ($RMSD_{tetrad}$, tetrad planarity and h-bond pattern) with respect the 'neutral' parent compound (**Fig. S15**, **Tables S25-S27**). In one case, for $G8^+$, located in the 'central' tetrad, the increase of the electrostatic repulsion with the two K^+ ions, leads to the 'leaking' of one of the K^+ towards the solvent and, consequently, to a large structural instability of the lower tetrad. The minimization of the electrostatic repulsions G^+/K^+ thus appears a major driving force for the structural rearrangements, as suggested by the increases of the average distance to the inner K^+ ion following G ionization (**Table S28**). Another important factor is the maximization of the G^+/solvent interactions. MD simulations indeed predict that, whatever its location, G^+ is better exposed to the solvent then G (**Tables S29-S30**).

4. Discussion

Guanine-rich sequences are prone to form G4 structures and at the same time undergo oxidative damage.[12, 13, 17] Guanine cation (G^+) is a key intermediate in many of these processes,[14] which can be triggered not only by an external oxidizing agent but also by the mere absorption of light, even in the UVB/UVA.[9] Each oxidative process follows a different mechanism, which is strongly modulated by a 'direct' interaction of the oxidizer and the base.[9] For what concerns 'direct' ionization, it has been suggested that an excited electronic state with significant charge transfer (CT) character is a key intermediate.[32, 87] It is thus clear that each process would require a specifically-tailored study, and, therefore, characterizing the formation of G^+ falls well outside the aim of this paper. We are instead interested in restricting our analysis to the G4 already containing the positive charge. Indeed, it is known that the positive charge on G^+ can quite rapidly migrate within DNA to the base with the lowest ionization potential.[88, 89] At the same time, time resolved (TR)

experiments on G4, starting from that carried out on Tel21/Na^+, show that G^+ can survive on the millisecond time-scale,[16, 17] i.e. enough to potentially induce a substantial structural rearrangement in the G4. Focusing on Tel21/Na^+, which adopts a basket-type topology (**Fig. 1**), we combine QM/MM calculations and MD simulations to study the structural shifts induced by the presence of a G^+ in one of the twelve G bases. Additionally, we check whether our conclusions hold for another folding topology (hybrid-1) in the presence of K^+.

QM/MM calculations on Tel21/Na^+ indicate that, whatever the position, the charge is essentially localized on a single G base, tends to repel the inner Na^+ ions and to perturb the regular h-bonding pattern of a tetrad. MD simulations show that $Tel21^+$ sequences keep a similar fold to the neutral species and in most of them the eleven G and the single G^+ bases are arranged in three 'regular' tetrads. This is a first important indication: the presence of a G^+ base is fully compatible with a quadruple helix, in line with its low oxidation potential.

However, the presence of a G^+ perturbs the structural behaviour of Tel21 and such a perturbation dramatically depends on the location of G^+. When G^+ is in tetrad2 or tetrad3, we observe minor structural rearrangements, which generally increase the solvent exposed surface and the average distance between the inner Na^+ ions and G^+. The most dramatic changes occur when G^+ is in tetrad1. Whatever the conformation of DL is, we often observe disruption of the tetrad h-bonding and swinging out of one or two bases. In particular, the most severe effects are observed when the cationic base is G13, G21 or G1.

Our simulations provide useful indications on the effects responsible of these structural shifts. One major driving force for all the conformational rearrangements is the electrostatic repulsion of G^+ and the inner ions. In all our simulations of $Tel21^+$, as well as in the QM/MM optimized structures, it turns out that, invariably, the average distance between G^+ and the Na^+ ions increases (**Table 1, Table S3, Table S12**). The formation of G^+ introduces an extra positive charge in the 'interior' of a G4, where two cations are already present. At the same time, the electron-donating power of the carbonyl Oxygen atoms (O6) decreases, since magnitude of their partial negative charge is significantly smaller in G^+ than in G.

In some simulations with the largest disruption of the G4 arrangement, we have also found a sporadic movement of the Na^+ ion out of the space between two tetrads. For instance, it occurs in both $Tel21G13^+$ and $Tel21G21^+$ systems (**Fig. S14**). In these simulations, due to the shifts of G13 and G21 bases away from the tetrad array, the Na^+1 ion gets closer to tetrad2, increasing the repulsion with Na^+2, which sporadically moves towards the LL. This is another key result, suggesting that, on a longer time scale, the stability of the G4, which critically depends on the presence of inner metal ions, could be weakened.

The tendency of G^+ to increase its solvent exposed surface appears to be another important driving force in our MD simulations.

Simulations of Tel21/K^+ support the reliability of our interpretative framework. G^+ perturbs the structural dynamics of Tel21/K^+, leading in some cases to significant structural rearrangements, which appears to be mainly driven by the minimization of the G^+/K^+ electrostatic repulsions and the maximization of G^+/water interactions.

4.1. Structural effects on Tel21 reactivity in oxidative processes.

In this section, we try to assess how the inclusion of G^+ at different positions in a G4 of a given topology affects the reactivity in the possible oxidative processes. First, we observe a striking

difference with respect to isolated dG in water, for which H1 deprotonation is strongly favored.[14, 18] G^+ in a G4 can instead undergo deprotonation also in the amino group (G-H2).[13, 16, 17] Actually, for the G^+ species directly produced by one-photon ionization (i.e. without the intervention of oxidizing agents) its formation is kinetically favored with respect to that of G-H1.[13, 16, 17] Moreover, as discussed by Fleming and Burrows in a fundamental contribution,[51] when a human telomeric sequence with 25 nucleotides (Tel25) arranged in a quadruple helix is exposed to different chemical oxidizing agents, striking differences with respect to the oxidative processes occurring in B-form duplex DNA are observed. In the presence of one-electron oxidizing agents, two different reaction pathways are identified. One, leading to 8-oxo-G and to the species produced by its further oxidation, is started by a water attack to G^+ at the C8 position.[51, 90] The other involves, as first step, the attack of $O2^{\bullet-}$ to the deprotonated G-H radical (which in the free base occurs at N1, i.e. G-H1).[9, 51, 91-93] Though the outcome of the process depends on the oxidizing agents employed, the reactivity of the different positions shows interesting trends. One-electron oxidizing agents preferentially attack the base at the 5'-end [51, 94-96] of each GGG sequence (i.e. G3, G9, G15, and G21 in their Tel25 sequence, corresponding to G1, G7, G13 and G19 in our study).

When the oxidizing agent is $^1O_2$, the more reactive sites are those in tetrad1 and tetrad3.[51] These general conclusions are valid for different G4 topologies, but the reactivity of the different positions shows some interesting features. To allow for an easier comparison of our simulations with the experimental results, the bases in the Tel25/Tel24 sequence will be reported in italics. Using riboflavin as oxidizing agent in basket-type fold, two positions in the basket-type fold (*G3*/G1 and *G15*/G13) stand out as the most reactive, three/four times more reactive than the two other positions at the 5'-end (*G9*/G7 and *G21*/G19), whereas *G9* is largely the most reactive site for the hybrid-2 and hybrid-1 folds, followed by *G3*/G1. It is also noteworthy that riboflavin is the agent for which the production of 2,2,4-triamino-2H-oxazol-5-one (Z) is the largest.[51] The process leading to Z formation is believed to involve a deprotonated G-H1 radical. Several factors can thus affect the reactivity of the different sites in the oxidative processes. Focusing on the processes involving a G^+ intermediate, we shall briefly discuss the most general ones, i.e. excluding the effects more related to the specific oxidizing agents and/or the specific folding topology of the G4,[97] which would require an ad-hoc study.

i) *Charge localization*. After G is ionized, by directly absorbing UV radiation or due to the action of a one-electron oxidizer, the hole can in principle rapidly migrate towards the bases with the lowest ionization potential. Studies on DNA single strand and duplex suggest that within a stacked G trimer, charge localization occurs preferentially at the 5'-end and at the middle base.[98-103] This observation could explain the reactivity trend observed in Tel25, considering that in G4 hole localization in the 'middle' G base is disfavored by the proximity of the two inner cations.[51] Experiments on duplex/quadruplex conjugate containing a rhodium-based photooxidant however show that damage is observed almost exclusively at the external tetrads of the quadruplex, without a clear preference for the 5'-end bases,[94] but it is possible that the dye can trigger many different oxidative pathways. Our study cannot give any firm indications on the role played by preferential hole localization at the 5' for G4. On the other hand, MD simulations suggest that solvent exposure and distance from the cations are important effects to determine charge localization, suggesting that it should be favored for tetrad1, followed by tetrad3, and strongly disfavored in tetrad2. These results can be likely related to the observed small reactivity of the middle tetrad in oxidative reactions. Some interesting results are obtained also for what concerns the different reactivity of the sites within tetrad 1 and tetrad3. For example, G7 of Tel21 is the most solvated base of tetrad3,

whereas G3 and G15 are the least exposed, suggesting that charge localization in the former base is more likely (**Table 2**). Similar trends are observed for the hybrid-1 fold with K^+. On the other hand, it is clear that, in addition to the probability of localizing the hole at a given position, it is important to analyze the possible reactive paths of G^+.

ii) *H1 vs H2 deprotonation*. Our MD simulations confirm that one of the amino protons (H2) is much more readily accessible to water than the H1 proton. Moreover, a substantial increase of the exposure of N1-H1 requires a significant rearrangement of the $Tel21^+$ structure. Both these indications are fully consistent with the faster formation of G-H2 found by TR experiments: in Tel21, G-H2 appears on a few μs time scale, and decays with a time-constant ∼1 ms .[16, 17] G-H1 appears instead on a ms time-scale.[16, 17] Incidentally, we are not aware of studies verifying whether -H2 deprotonation can trigger different photochemical processes than -H1 deprotonation, but we cannot take for granted that they are the same. Moreover, based on our simulations, we can expect that the deprotonation rate could exhibit complex trends, with some positions deprotonating at faster rates, and others, those requiring more substantial rearrangements, at slower rates. This behavior is fully consistent with the results of TR experiments on Tel21, with a part of the G^+ population lost on the μs time scale and another part decaying on the ms one.[16, 17]

Interestingly, our MD simulations suggest that the relative propensity of G^+ to undergo -H2 or -H1 deprotonation depends on the position, which severely affects water accessibility to the acidic protons. For example, some G^+ positions display relatively frequent N1-H1/solvent interactions: this occurs for G1 and G7 (whose N1-H1 are already partially exposed in neutral Tel21), as well as for G13, G21, and G3. Interestingly, G1, G7, and G13 have been found to be particularly reactive towards oxidative damage in $Tel25/Na^+$. In particular, the high solvent exposure of N1-H1 for G1 and G13 could be related to their relatively larger yield of Z, which is believed to require H1 deprotonation in the presence of riboflavin.[51] Only detailed study of this reaction, considering the possible fast H2/H1 tautomerization reaction, would however be necessary to firmly assess this issue.

iii) *Structural stability of the cation*. Most of the above considerations are strictly valid in the limit that G^+ formation does not drive any substantial structural rearrangement of Tel21. As discussed above, while for some positions, especially in tetrad2, we observe only minor asymmetrization of the h-bonding patterns, for others major rearrangements are predicted. In this respect, the flexibility of a given tract of the sequence is a key feature, which could play a major role in determining the reactivity. On the one hand, it could facilitate the access of the oxidizing species. On the other hand, the conformational rearrangements induced by the ionization could be easier. The system would rapidly move to another conformational arrangement, more suitable for a positively charged base in that position, decreasing the possibility of hole transfer to other bases. Again, the bases undergoing the largest shifts upon ionization are G1, G13, and G21 in tetrad1, and G3 and G7 in tetrad3.

iv) *Solvent exposure*. As also suggested in previous studies,[51, 104, 105] solvent exposure appears to be a key effect in driving both the localization of the hole to a certain position and its subsequent reactivity. We have shown that simple analysis of solvent exposure of different bases in a given fold can give important preliminary insights on the reactivity trends (e.g., bases in tetrad1 of $Tel21/Na^+$ are more solvent exposed and more reactive than those in tetrad2, or similarly, the two most reactive positions towards one-electron oxidizing agents in $Tel21/K^+$ are those more exposed to the solvent (**Table S29**)).

In addition to the 'global' solvent exposure, it is important to analyze in detail also the interaction with the solvent of the different moieties of G^+. Any chemical reaction involving G^+ and the water molecules, from the deprotonation to the attack at the C8 position of G^+, indeed requires the interaction of water with specific base groups in specific arrangements. For example, we could have a G^+ quite exposed to the solvent (and thus favoring localization of the hole), but its C8 group is, at the same time, shielded from the interaction with the solvent. This is the case of $G8^+$ and $G15^+$, which are rather solvent exposed (cfr. **Table 2** with **Tables S22, S24**). Moreover, all the *syn* G^+ in the basket topology contain more solvent exposed C8 groups compared to *anti* G^+, with the only exception of $G2^+$ (see **Tables S22, S24**).

Another key point to be analyzed is the possible presence of water access pathways in the structure. It is important for any occurring reaction (e.g., the deprotonation), since additional water molecules could play an important catalytic role. Moreover, it is a hint of possible ways of access of oxidizing agents. For instance, due to both the flexible A6 base and the A:T pairing between A18 and T5 (**Table S7**), which stack on tetrad3 (especially G3 and G15), the approaching of water molecules to the N1 atoms of tetrad3 bases are not the same for the four bases. Indeed, only for G7 base, water molecules facing N1-H1 groups have rather free access (**Table S17**) and a shift of G7 out of the tetrad3 plane could easily points G7 N1 atom towards water molecules, thus contributing to the higher reactivity of the *G9*/G7 position in Tel25.[51]

v) *Conformational behavior of the loops*. The conformational behavior of the loops modulates many of the effects discussed above. For example, the solvent exposure of tetrad1 strongly depends on the DL conformation. Moreover, DL is the most constrained, contributing to the dramatic conformational rearrangements observed in tetrad1 for $Tel21^+$. Loops can also interact with the bases present at the 3'- and 5'-end as shown, for example, by the comparison between Tel21 and Tel22. Loop bases can also play a key role in any conformational rearrangements observed in $Tel21^+$, establishing transient or stable interactions with the Gs. Shortly, the conformational behavior of the loop is not anodyne with respect to the reactivity of G^+. On the one hand, this provides an additional route for the control of the damage. Just to make an example, it could be possible to modulate the photoactivated reactivity of a base in G4 by using a compound/drug stabilizing a given arrangement of the loop. On the other hand, this calls for additional studies improving the quality of the force field in modeling the conformational behavior of the loops.[42, 106]

vi) *Charged moieties: ions and phosphate groups*. Inner cations also affect the reactivity trends within a G4.[17, 30] As discussed above, they contribute to decrease the reactivity of the central tetrads of a given fold, disfavoring the localization of the positive charge. Interestingly, the possibility of increasing the distance from the inner ions is not the same for all the positions in tetrad1 and tetrad3. For example, in tetrad3, G3 and G7 reach a larger distance from Na^+2 than the other two bases. Analogously, in tetrad1, $G9^+$ is closer to Na^+1 than the other three bases.

The mobility of the ion could play a role, too. For example, the inner cations tend to move farther from G^+ and, in two cases ($Tel21G13^+$ and $Tel21G21^+$), we find that the ion moves out of the Tel21 inter-tetrad space (tetrad2-tetrad3). Consequently, we can expect that a less mobile ion than Na^+ can affect the reactivity at different level (besides altering the folding topology of the G4). This prediction is confirmed by the simulations performed in the presence of K^+. This cation is bulkier than Na^+ and, therefore, it has a more limited mobility in the 'intra-tetrad' space. As a consequence, when G^+ is located in the 'central' tetrad, which is sandwiched between two K^+ ions, the only way to decrease the strong electrostatic repulsion is to 'expel' one of the K^+ ion from the G4.

vii) *System dependent effects:* All the effects we have discussed above depend on the particular fold adopted by Tel21 and Tel22 in the presence of Na^+ and, at the same time, the MD simulations we performed are strictly valid only for the systems we have investigated. Nonetheless, they provide useful indications on the critical points to be assessed when trying to translate our conclusions to other systems, as confirmed by the simulations of hybrid-1 with K^+. A key issue concerns the length of the sequence under study. Even in the case for which no significant change in the fold is observed, the presence of additional bases at the 5'- or 3'-end can affect the reactivity of the bases, especially those of the outer tetrads. In this respect, the comparison between the behavior of Tel21/Na^+ and Tel22/Na^+ can be very informative. The presence of an additional base (A0) at the 5'-end significantly shields not only G1 (which is directly bonded to A0), but also G13, partially covered by the G1 phosphate. Analogously, we can expect that in Tel25 the presence of additional two bases at the 3'-end decreases the solvent exposure of at least G21, altering its reactivity. Moreover, the access of the solvent to H1 protons could be more complicated, as demonstrated by the absence of -H1 deprotonation found in tetramolecular parallel G4 formed by the sequence TGGGGT in the presence of K^+.[17]
A schematic drawing of the different effects discussed above is shown in **Fig. 8**.

5. Conclusions

The ionization of G base and, thus, the formation of G^+ is one of the first and key steps in many oxidative reactions endangering the genetic code of living beings.[12, 13] Such a process is known to be easier for sequences containing many closely stacked bases, as those forming G4. The lifetime of G^+ (in the μs-ms range) is long enough to make it extremely important to get detailed insights on the effect that G^+ has on the structure of G4s. Attaining such a goal using experimental techniques is not trivial, because of the tendency of G^+ to deprotonate and the small 'local concentration' of G^+ in experiments performed in 'physiological' conditions. In this study, we thus resorted to a computational approach, combining QM calculations and MD simulations, to study one of the most important G4-forming sequences, a 21 base-long tract of human telomeric sequence (Tel21) in anti-parallel basket topology in the presence of Na^+ ions. The QM/MM calculations indicate that the hole is essentially localized on a single base irrespective of its position in the structure, i.e. there is one G^+ base and 11 'almost neutral' Gs. This result cannot be taken for granted for G4, since for some topologies partial hole delocalization (i.e. two bases bearing a partial positive charge) is possible.[31] The MD simulations of the neutral Tel21 (10 independent simulations) and twelve $Tel21^+$ systems (a total of 20 simulations) differing for the location of the G^+ base indicate that G^+ provokes a substantial structural rearrangement when located in one of the four bases adjacent to the DL (tetrad1), with a G base moving out of the tetrad plane in three positions (G1, G13, and G21, using the Tel21 numbering). Significant structural shifts are predicted also for two positions (G3 and G7) of the tetrad3, the one close to the LLs. When G^+ is located in the inner tetrad we observe only minor shifts in the h-bonding pattern. Our simulations allow us to highlight the main driving forces for these shifts, which could also rule the preferential localization of a hole formed within Tel21. The onset of electrostatic repulsion between G^+ and the inner Na^+ ions is expected to play a major role, as well as the solvent exposure of the different positions. Finally, the local flexibility of the G4 tracts is important, too. On this ground, we can predict which positions are more prone to undergo oxidative damage and define some reactivity trends that, overall, are consistent with the experimental indications. It is clear that any oxidative reaction is ruled by different factors and

deserves a purposely-tailored study. Analogously, for what concerns other topologies, only the analysis of a given fold and sequence can give firm indication on the reactivity of the different sites. Our tests on Tel21 adopting the hybrid-1 fold in the presence of K^+ fully confirm the main conclusions obtained on Tel21/Na^+, revealing that the main chemical/physical effects we have evidenced are operative with different folding topologies/ions. For the first time, we here thus provide an atomistic picture of the early steps of oxidative damage in DNA and we expect that the key factors highlighted in the present study are operative also in other folds and can guide the interpretation of the observed trends, both in biomedical and nanotechnological applications.

Acknowledgments

This work has received funding from the European Union's Horizon 2020 research and innovation programme under the Marie Skodowska-Curie grant agreement No 765266 (LightDyNAmics). The work was also supported by the project 21-23718S from Czech Science Foundation (JS and PS) and by project SYMBIT reg. number: CZ.02.1.01/0.0/0.0/15_003/0000477 financed by the ERDF (JS). L.M.F. thanks the PID2019-110091GB-I00 (MICINN) project for financial support and the Centro de Computación Científica UAM (CCC-UAM) for computing time. The authors thank Prof. C. Burrows and Prof. A. Fleming (University of Utah) for very helpful discussions.

References

[1] S. Neidle, S. Balasubramanian, Quadruplex Nucleic Acids. (2006).
[2] D. Yang, C. Lin, G-Quadruplex Nucleic Acids: Methods and Protocols Humana, New York, NY, (2019).
[3] G. Biffi, D. Tannahill, J. McCafferty, S. Balasubramanian, Quantitative visualization of DNA G-quadruplex structures in human cells, Nat. Chem. 5 (2013) 182-186.
[4] D. Rhodes, H.J. Lipps, G-quadruplexes and their regulatory roles in biology, Nucleic Acids Res. 43 (2015) 8627-8637.
[5] J. Spiegel, S. Adhikari, S. Balasubramanian, The Structure and Function of DNA G-Quadruplexes, Trends Chem. 2 (2020) 123-136.
[6] D. Varshney, J. Spiegel, K. Zyner, D. Tannahill, S. Balasubramanian, The regulation and functions of DNA and RNA G-quadruplexes, Nat. Rev. Mol. Cell Biol. 21 (2020) 459-474.
[7] S. Balasubramanian, L.H. Hurley, S. Neidle, Targeting G-quadruplexes in gene promoters: a novel anticancer strategy?, Nat. Rev. Drug Discov. 10 (2011) 261-275.
[8] P. Martinez, M.A. Blasco, Telomere-driven diseases and telomere-targeting therapies, J. Cell Biol. 216 (2017) 875-887.
[9] J. Cadet, T. Douki, J.L. Ravanat, Oxidatively generated damage to the guanine moiety of DNA: mechanistic aspects and formation in cells, Acc. Chem. Res. 41 (2008) 1075-1083.
[10] E. Meggers, M.E. Michel-Beyerle, B. Giese, Sequence Dependent Long Range Hole Transport in DNA, J. Am. Chem. Soc. 120 (1998) 12950-12955.
[11] I. Saito, T. Nakamura, K. Nakatani, Y. Yoshioka, K. Yamaguchi, H. Sugiyama, Mapping of the Hot Spots for DNA Damage by One-Electron Oxidation: Efficacy of GG Doublets and GGG Triplets as a Trap in Long-Range Hole Migration, J. Am. Chem. Soc. 120 (1998) 12686-12687.
[12] J. Choi, J. Park, A. Tanaka, M.J. Park, Y.J. Jang, M. Fujitsuka, et al., Hole Trapping of G-Quartets in a G-Quadruplex, Angew. Chem. Int. Ed. 52 (2013) 1134-1138.
[13] L. Wu, K. Liu, J. Jie, D. Song, H. Su, Direct Observation of Guanine Radical Cation Deprotonation in G-Quadruplex DNA, J. Am. Chem. Soc. 137 (2015) 259-266.
[14] L.P. Candeias, S. Steenken, Ionization of purine nucleosides and nucleotides and their components by 193-nm laser photolysis in aqueous solution: model studies for oxidative damage of DNA, J. Am. Chem. Soc. 114 (1992) 699-704.
[15] M. Gomez-Mendoza, A. Banyasz, T. Douki, D. Markovitsi, J.-L. Ravanat, Direct Oxidative Damage of Naked DNA Generated upon Absorption of UV Radiation by Nucleobases, J. Phys. Chem. Lett. 7 (2016) 3945-3948.

[16] A. Banyasz, L. Martínez-Fernández, C. Balty, M. Perron, T. Douki, R. Improta, et al., Absorption of Low-Energy UV Radiation by Human Telomere G-Quadruplexes Generates Long-Lived Guanine Radical Cations, J. Am. Chem. Soc. 139 (2017) 10561-10568.
[17] E. Balanikas, A. Banyasz, T. Douki, G. Baldacchino, D. Markovitsi, Guanine Radicals Induced in DNA by Low-Energy Photoionization, Acc. Chem. Res. 53 (2020) 1511-1519.
[18] L.P. Candeias, S. Steenken, Stucture and acid-base properties of one-electron-oxidized deoxyguanosine, guanosine, and 1-methylguanosine, J. Am. Chem. Soc. 111 (1989) 1094-1099.
[19] J. Cadet, F. Odin, J.F. Mouret, M. Polverelli, A. Audic, P. Giacomoni, et al., Chemical and biochemical postlabeling methods for singling out specific oxidative DNA lesions, Mutat. Res. 275 (1992) 343-354.
[20] W.L. Neeley, J.M. Essigmann, Mechanisms of Formation, Genotoxicity, and Mutation of Guanine Oxidation Products, Chem. Res. Toxicol. 19 (2006) 491-505.
[21] R.K. Moyzis, J.M. Buckingham, L.S. Cram, M. Dani, L.L. Deaven, M.D. Jones, et al., A highly conserved repetitive DNA sequence, (TTAGGG)n, present at the telomeres of human chromosomes, Proc. Natl. Acad. Sci. U.S.A. 85 (1988) 6622.
[22] J. Meyne, R.L. Ratliff, R.K. Moyzis, Conservation of the human telomere sequence (TTAGGG)n among vertebrates, Proc. Natl. Acad. Sci. U.S.A. 86 (1989) 7049.
[23] E.H. Blackburn, Telomere states and cell fates, Nature 408 (2000) 53-56.
[24] G.I. Livshits, A. Stern, D. Rotem, N. Borovok, G. Eidelshtein, A. Migliore, et al., Long-range charge transport in single G-quadruplex DNA molecules, Nature Nanotech. 9 (2014) 1040-1046.
[25] J.-L. Mergny, D. Sen, DNA Quadruple Helices in Nanotechnology, Chem. Rev. 119 (2019) 6290-6325.
[26] L.A. Yatsunyk, O. Mendoza, J.-L. Mergny, "Nano-oddities": Unusual Nucleic Acid Assemblies for DNA-Based Nanostructures and Nanodevices, Acc. Chem. Res. 47 (2014) 1836-1844.
[27] C.J. Lech, P. Anh Tuan, M.-E. Michel-Beyerle, A.A. Voityuk, Electron-Hole Transfer in G-Quadruplexes with Different Tetrad Stacking Geometries: A Combined QM and MD Study, J. Phys. Chem. B 117 (2013) 9851-9856.
[28] H. Gattuso, A. Spinello, A. Terenzi, X. Assfeld, G. Barone, A. Monari, Circular Dichroism of DNA G-Quadruplexes: Combining Modeling and Spectroscopy To Unravel Complex Structures, J. Phys. Chem. B 120 (2016) 3113-3121.
[29] A. Banyasz, E. Balanikas, L. Martínez-Fernández, G. Baldacchino, T. Douki, R. Improta, et al., Radicals Generated in Tetramolecular Guanine Quadruplexes by Photoionization: Spectral and Dynamical Features, J. Phys. Chem. B 123 (2019) 4950-4957.
[30] B. Behmand, E. Balanikas, L. Martínez-Fernández, R. Improta, A. Banyasz, G. Baldacchino, et al., Potassium Ions Enhance Guanine Radical Generation upon Absorption of Low-Energy Photons by G-Quadruplexes and Modify Their Reactivity, J. Phys. Chem. Lett. 11 (2020) 1305-1309.
[31] L. Martínez-Fernández, A. Banyasz, D. Markovitsi, R. Improta, Topology Controls the Electronic Absorption and Delocalization of Electron Holes in Guanine Quadruplexes, Chem. Eur. J. 24 (2018) 15185-15189.
[32] L. Martínez-Fernández, P. Changenet, A. Banyasz, T. Gustavsson, D. Markovitsi, R. Improta, Comprehensive Study of Guanine Excited State Relaxation and Photoreactivity in G-quadruplexes, J. Phys. Chem. Lett. 10 (2019) 6873-6877.
[33] M. Deiana, B. Mettra, L. Martínez-Fernández, L.M. Mazur, K. Pawlik, C. Andraud, et al., Specific Recognition of G-Quadruplexes Over Duplex-DNA by a Macromolecular NIR Two-Photon Fluorescent Probe, J. Phys. Chem. Lett. 8 (2017) 5915-5920.
[34] D. Loco, S. Jurinovich, L.D. Bari, B. Mennucci, A fast but accurate excitonic simulation of the electronic circular dichroism of nucleic acids: how can it be achieved?, Phys. Chem. Chem. Phys. 18 (2016) 866-877.
[35] W. Lee, S. Matsika, Conformational and electronic effects on the formation of anti cyclobutane pyrimidine dimers in G-quadruplex structures, Phys. Chem. Chem. Phys. 19 (2017) 3325-3336.
[36] C. Nieuwland, F. Zaccaria, C. Fonseca Guerra, Understanding alkali metal cation affinities of multi-layer guanine quadruplex DNA, Phys. Chem. Chem. Phys. 22 (2020) 21108-21118.
[37] J. Zhou, B.T. Roembke, G. Paragi, A. Laguerre, H.O. Sintim, C. Fonseca Guerra, et al., Computational understanding and experimental characterization of twice-as-smart quadruplex ligands as chemical sensors of bacterial nucleotide second messengers, Sci. Rep. 6 (2016) 33888.
[38] F. Zaccaria, G. Paragi, C. Fonseca Guerra, The role of alkali metal cations in the stabilization of guanine quadruplexes: why K+ is the best, Phys. Chem. Chem. Phys. 18 (2016) 20895-20904.

[39] D. Avagliano, P.A. Sánchez-Murcia, L. González, Spiropyran Meets Guanine Quadruplexes: Isomerization Mechanism and DNA Binding Modes of Quinolizidine-Substituted Spiropyran Probes, Chem. Eur. J. 26 (2020) 13039-13045.
[40] D. Avagliano, S. Tkaczyk, P.A. Sánchez-Murcia, L. González, Enhanced Rigidity Changes Ultraviolet Absorption: Effect of a Merocyanine Binder on G-Quadruplex Photophysics, J. Phys. Chem. Lett. 11 (2020) 10212-10218.
[41] J. Šponer, X. Cang, T.E. Cheatham, Molecular dynamics simulations of G-DNA and perspectives on the simulation of nucleic acid structures, Methods 57 (2012) 25-39.
[42] B. Islam, P. Stadlbauer, M. Krepl, M. Havrila, S. Haider, J. Šponer, Structural Dynamics of Lateral and Diagonal Loops of Human Telomeric G-Quadruplexes in Extended MD Simulations, J. Chem. Theory Comput. 14 (2018) 5011-5026.
[43] M. Rebič, A. Laaksonen, J. Šponer, J. Uličný, F. Mocci, Molecular Dynamics Simulation Study of Parallel Telomeric DNA Quadruplexes at Different Ionic Strengths: Evaluation of Water and Ion Models, J. Phys. Chem. B 120 (2016) 7380-7391.
[44] J.A. Lemkul, Same fold, different properties: polarizable molecular dynamics simulations of telomeric and TERRA G-quadruplexes, Nucleic Acids Res. 48 (2020) 561-575.
[45] P. Stadlbauer, P. Kührová, L. Vicherek, P. Banáš, M. Otyepka, L. Trantírek, et al., Parallel G-triplexes and G-hairpins as potential transitory ensembles in the folding of parallel-stranded DNA G-Quadruplexes, Nucleic Acids Res. 47 (2019) 7276-7293.
[46] J. Šponer, N.a. Špačková, Molecular dynamics simulations and their application to four-stranded DNA, Methods 43 (2007) 278-290.
[47] B. Islam, M. Sgobba, C. Laughton, M. Orozco, J. Šponer, S. Neidle, et al., Conformational dynamics of the human propeller telomeric DNA quadruplex on a microsecond time scale, Nucleic Acids Res. 41 (2013) 2723-2735.
[48] T. Siebenmorgen, M. Zacharias, Origin of Ion Specificity of Telomeric DNA G-Quadruplexes Investigated by Free-Energy Simulations, Biophys. J. 112 (2017) 2280-2290.
[49] Y. Wang, D.J. Patel, Solution structure of the human telomeric repeat d[$AG_3(T_2AG_3)_3$] G-tetratraplex, Structure 1 (1993) 263-282.
[50] K.N. Luu, A.T. Phan, V. Kuryavyi, L. Lacroix, D.J. Patel, Structure of the Human Telomere in K+ Solution: An Intramolecular (3 + 1) G-Quadruplex Scaffold, J. Am. Chem. Soc. 128 (2006) 9963-9970.
[51] A.M. Fleming, C.J. Burrows, G-Quadruplex Folds of the Human Telomere Sequence Alter the Site Reactivity and Reaction Pathway of Guanine Oxidation Compared to Duplex DNA, Chem. Res. Toxicol. 26 (2013) 593-607.
[52] M. Vorlickova, J. Chladkova, I. Kejnovska, M. Fialova, J. Kypr, Guanine tetraplex topology of human telomere DNA is governed by the number of (TTAGGG) repeats, Nucleic Acids Res. 33 (2005) 5851-5860.
[53] D. Renciuk, I. Kejnovska, P. Skolakova, K. Bednarova, J. Motlova, M. Vorlickova, Arrangements of human telomere DNA quadruplex in physiologically relevant K+ solutions, Nucleic Acids Res. 37 (2009) 6625-6634.
[54] M. Vorlickova, I. Kejnovska, J. Sagi, D. Renciuk, K. Bednarova, J. Motlova, et al., Circular dichroism and guanine quadruplexes, Methods 57 (2012) 64-75.
[55] Y. Zhao, N.E. Schultz, D.G. Truhlar, Design of density functionals by combining the method of constraint satisfaction with parametrization for thermochemistry, thermochemical kinetics, and noncovalent interactions, J. Chem. Theory Comput. 2 (2006) 364-382.
[56] W.D. Cornell, P. Cieplak, C.I. Bayly, I.R. Gould, K.M. Merz, D.M. Ferguson, et al., A 2nd generation force-field for the simulation of proteins, nucleic acids, and organic molecules, J. Am. Chem. Soc. 117 (1995) 5179-5197.
[57] S. Dapprich, I. Komaromi, K.S. Byun, K. Morokuma, M.J. Frisch, A new ONIOM implementation in Gaussian98. Part I. The calculation of energies, gradients, vibrational frequencies and electric field derivatives, J. Mol. Struct.-Theochem 461 (1999) 1-21.
[58] J. Tomasi, B. Mennucci, R. Cammi, Quantum mechanical continuum solvation models, Chem. Rev. 105 (2005) 2999-3093.
[59] S. Miertus, E. Scrocco, J. Tomasi, Electrostatic interaction of a solute with a continuum - A direct utilization of abinitio molecular potentials for the prevision of solvent effects Chem. Phys. 55 (1981) 117-129.
[60] M.J. Frisch et al., (Gaussian 09, revision A.1; Gaussian, Inc.,Wallingford, CT, 2009).

[61] T. Wilson, P.J. Costa, V. Felix, M.P. Williamson, J.A. Thomas, Structural studies on dinuclear ruthenium(II) complexes that bind diastereoselectively to an antiparallel folded human telomere sequence, J. Med. Chem. 56 (2013) 8674-8683.
[62] D. Case, R. Betz, D. Cerutti, T. Cheatham III, T. Darden, R. Duke, et al. AMBER 2016. San Francisco: University of California; 2016.
[63] M. Zgarbová, J. Šponer, M. Otyepka, T.E. Cheatham, R. Galindo-Murillo, P. Jurečka, Refinement of the Sugar-Phosphate Backbone Torsion Beta for AMBER Force Fields Improves the Description of Z- and B-DNA, J. Chem. Theory Comput. 11 (2015) 5723.
[64] R. Galindo-Murillo, J.C. Robertson, M. Zgarbová, J. Šponer, M. Otyepka, P. Jurečka, et al., Assessing the Current State of Amber Force Field Modifications for DNA, J. Chem. Theory Comput. 12 (2016) 4114.
[65] J.M. Wang, P. Cieplak, P.A. Kollman, How well does a restrained electrostatic potential (RESP) model perform in calculating conformational energies of organic and biological molecules?, J. Comput. Chem. 21 (2000) 1049-1074.
[66] H.J.C. Berendsen, J.R. Grigera, T.P. Straatsma, The Missing Term in Effective Pair Potentials, J. Phys. Chem. 91 (1987) 6269-6271.
[67] I.S. Joung, T.E. Cheatham, Determination of alkali and halide monovalent ion parameters for use in explicitly solvated biomolecular simulations, J. Phys. Chem. B 112 (2008) 9020-9041.
[68] M. Havrila, P. Stadlbauer, B. Islam, M. Otyepka, J. Šponer, Effect of Monovalent Ion Parameters on Molecular Dynamics Simulations of G-Quadruplexes, J. Chem. Theory Comput. 13 (2017) 3911-3926.
[69] T. Darden, D. York, L. Pedersen, Particle Mesh Ewald: An N·log(N) Method for Ewald Sums in Large Systems, J. Chem. Phys. 98 (1993) 10089.
[70] W. Humphrey, A. Dalke, K. Schulten, VMD: Visual Molecular Dynamics, J. Mol. Graphics 14 (1996) 33.
[71] Schrodinger, LLC. The PyMOL Molecular Graphics System, Version 1.8. 2015.
[72] D.R. Roe, T.E. Cheatham, PTRAJ and CPPTRAJ: Software for Processing and Analysis of Molecular Dynamics Trajectory Data, J. Chem. Theory Comput. 9 (2013) 3084.
[73] X.-J. Lu, H.J. Bussemaker, W.K. Olson, DSSR: an integrated software tool for dissecting the spatial structure of RNA, Nucleic Acids Res. 43 (2015) e142-e142.
[74] X.-J. Lu, W.K. Olson, 3DNA: a versatile, integrated software system for the analysis, rebuilding and visualization of three-dimensional nucleic-acid structures, Nat. Protoc. 3 (2008) 1213-1227.
[75] M. Nakano, H. Tateishi-Karimata, S. Tanaka, N. Sugimoto, Affinity of Molecular Ions for DNA Structures Is Determined by Solvent-Accessible Surface Area, J. Phys. Chem. B 118 (2014) 9583-9594.
[76] M. Nakano, H. Tateishi-Karimata, S. Tanaka, N. Sugimoto, Choline Ion Interactions with DNA Atoms Explain Unique Stabilization of A–T Base Pairs in DNA Duplexes: A Microscopic View, J. Phys. Chem. B 118 (2014) 379-389.
[77] D. Van Der Spoel, E. Lindahl, B. Hess, G. Groenhof, A.E. Mark, H.J. Berendsen, GROMACS: fast, flexible, and free, J. Comput. Chem. 26 (2005) 1701-1718.
[78] M. Egli, DNA-Cation Interactions: Quo Vadis?, Chem. Biol. 9 (2002) 277-286.
[79] J. Šponer, G. Bussi, M. Krepl, P. Banáš, S. Bottaro, R.A. Cunha, et al., RNA Structural Dynamics As Captured by Molecular Simulations: A Comprehensive Overview, Chem. Rev. 118 (2018) 4177-4338.
[80] H. Liu, R. Wang, X. Yu, F. Shen, W. Lan, P. Haruehanroengra, et al., High-resolution DNA quadruplex structure containing all the A-, G-, C-, T-tetrads, Nucleic Acids Res. 46 (2018) 11627-11638.
[81] M.P. Lee, G.N. Parkinson, P. Hazel, S. Neidle, Observation of the coexistence of sodium and calcium ions in a DNA G-quadruplex ion channel, J. Am. Chem. Soc. 129 (2007) 10106-10107.
[82] G. Laughlan, A.I. Murchie, D.G. Norman, M.H. Moore, P.C. Moody, D.M. Lilley, et al., The high-resolution crystal structure of a parallel-stranded guanine tetraplex, Science 265 (1994) 520.
[83] K. Phillips, Z. Dauter, A.I.H. Murchie, D.M.J. Lilley, B. Luisi, The crystal structure of a parallel-stranded guanine tetraplex at 0.95Å resolution, J. Mol. Biol. 273 (1997) 171-182.
[84] M.P. Horvath, S.C. Schultz, DNA G-quartets in a 1.86 Å resolution structure of an Oxytricha nova telomeric protein-DNA complex, J. Mol. Biol. 310 (2001) 367-377.
[85] E. Balanikas, A. Banyasz, G. Baldacchino, D. Markovitsi, Guanine Radicals Generated in Telomeric G-Quadruplexes by Direct Absorption of Low-Energy UV Photons: Effect of Potassium Ions, Molecules 25 (2020).
[86] I. Bessi, H.R.A. Jonker, C. Richter, H. Schwalbe, Involvement of Long-Lived Intermediate States in the Complex Folding Pathway of the Human Telomeric G-Quadruplex, Angew. Chem. Int. Ed. 54 (2015) 8444-8448.

[87] L. Martínez-Fernández, L. Esposito, R. Improta, Studying the excited electronic states of guanine rich DNA quadruplexes by quantum mechanical methods: main achievements and perspectives, Photochem. Photobiol. Sci. 19 (2020) 436-444.
[88] C.-S. Liu, R. Hernandez, G.B. Schuster, Mechanism for Radical Cation Transport in Duplex DNA Oligonucleotides, J. Am. Chem. Soc. 126 (2004) 2877-2884.
[89] J.C. Genereux, J.K. Barton, Mechanisms for DNA Charge Transport, Chem. Rev. 110 (2010) 1642-1662.
[90] D. Angelov, A. Spassky, M. Berger, J. Cadet, High-Intensity UV Laser Photolysis of DNA and Purine 2‘-Deoxyribonucleosides: Formation of 8-Oxopurine Damage and Oligonucleotide Strand Cleavage as Revealed by HPLC and Gel Electrophoresis Studies, J. Am. Chem. Soc. 119 (1997) 11373-11380.
[91] R. Misiaszek, C. Crean, A. Joffe, N.E. Geacintov, V. Shafirovich, Oxidative DNA damage associated with combination of guanine and superoxide radicals and repair mechanisms via radical trapping, J. Biol. Chem. 279 (2004) 32106-32115.
[92] M.M. Greenberg, The Formamidopyrimidines: Purine Lesions Formed in Competition With 8-Oxopurines From Oxidative Stress, Acc. Chem. Res. 45 (2012) 588-597.
[93] J. Cadet, M. Berger, G.W. Buchko, P.C. Joshi, S. Raoul, J.-L. Ravanat, 2,2-Diamino-4-[(3,5-di-O-acetyl-2-deoxy-.beta.-D-erythro- pentofuranosyl)amino]-5-(2H)-oxazolone: a Novel and Predominant Radical Oxidation Product of 3',5'-Di-O-acetyl-2'-deoxyguanosine, J. Am. Chem. Soc. 116 (1994) 7403-7404.
[94] S. Delaney, J.K. Barton, Charge transport in DNA duplex/quadruplex conjugates, Biochemistry 42 (2003) 14159-14165.
[95] T. Ndlebe, G.B. Schuster, Long-distance radical cation transport in DNA: horizontal charge hopping in a dimeric quadruplex, Org. Biomol. Chem. 4 (2006) 4015-4021.
[96] V.A. Szalai, M.J. Singer, H.H. Thorp, Site-Specific Probing of Oxidative Reactivity and Telomerase Function Using 7,8-Dihydro-8-oxoguanine in Telomeric DNA, J. Am. Chem. Soc. 124 (2002) 1625-1631.
[97] A.M. Fleming, A.M. Orendt, Y. He, J. Zhu, R.K. Dukor, C.J. Burrows, Reconciliation of Chemical, Enzymatic, Spectroscopic and Computational Data To Assign the Absolute Configuration of the DNA Base Lesion Spiroiminodihydantoin, J. Am. Chem. Soc. 135 (2013) 18191-18204.
[98] C.L. Cleveland, R.N. Barnett, A. Bongiorno, J. Joseph, C. Liu, G.B. Schuster, et al., Steric Effects on Water Accessability Control Sequence-Selectivity of Radical Cation Reactions in DNA, J. Am. Chem. Soc. 129 (2007) 8408-8409.
[99] H. Sugiyama, I. Saito, Theoretical Studies of GG-Specific Photocleavage of DNA via Electron Transfer: Significant Lowering of Ionization Potential and 5‘-Localization of HOMO of Stacked GG Bases in B-Form DNA, J. Am. Chem. Soc. 118 (1996) 7063-7068.
[100] D.B. Hall, J.K. Barton, Sensitivity of DNA-Mediated Electron Transfer to the Intervening π-Stack: A Probe for the Integrity of the DNA Base Stack, J. Am. Chem. Soc. 119 (1997) 5045-5046.
[101] D.T. Breslin, G.B. Schuster, Anthraquinone Photonucleases: Mechanisms for GG-Selective and Nonselective Cleavage of Double-Stranded DNA, J. Am. Chem. Soc. 118 (1996) 2311-2319.
[102] R.P. Hickerson, F. Prat, J.G. Muller, C.S. Foote, C.J. Burrows, Sequence and Stacking Dependence of 8-Oxoguanine Oxidation: Comparison of One-Electron vs Singlet Oxygen Mechanisms, J. Am. Chem. Soc. 121 (1999) 9423-9428.
[103] A. Kumar, A. Adhikary, M.D. Sevilla, D.M. Close, One-electron oxidation of ds(5’-GGG-3’) and ds(5’-G(8OG)G-3’) and the nature of hole distribution: a density functional theory (DFT) study, Phys. Chem. Chem. Phys. 22 (2020) 5078-5089.
[104] Y.-A. Lee, Z. Liu, P.C. Dedon, N.E. Geacintov, V. Shafirovich, Solvent exposure associated with single abasic sites alters the base sequence dependence of oxidation of guanine in DNA in GG sequence contexts, Chembiochem 12 (2011) 1731-1739.
[105] A.M. Fleming, J.G. Muller, A.C. Dlouhy, C.J. Burrows, Structural Context Effects in the Oxidation of 8-Oxo-7,8-dihydro-2’-deoxyguanosine to Hydantoin Products: Electrostatics, Base Stacking, and Base Pairing, J. Am. Chem. Soc. 134 (2012) 15091-15102.
[106] B. Islam, P. Stadlbauer, A. Gil-Ley, G. Pérez-Hernández, S. Haider, S. Neidle, et al., Exploring the Dynamics of Propeller Loops in Human Telomeric DNA Quadruplexes Using Atomistic Simulations, J. Chem. Theory Comput. 13 (2017) 2458-2480.

Table 1. Average distances (in Å) between O6 atoms of each base and Na^+ ions in cationic and neutral system simulations. The column 'Tel21 cations' reports values in the simulations where the respective base is charged. Tetrad bases and distances are depicted in red, black, and blue for tetrad1, tetrad2 and tetrad3, respectively. Values greater than 2.65 Å are denoted in italics and underlined; values greater than 3.0 Å are denoted in bold and underlined.

	Distance (Å)						
	Distance O6-Na^+1				Distance O6-Na^+2		
Base	Tel22	Tel21	Tel21 Cations	Base	Tel22	Tel21	Tel21 Cations
G1	2.52	*2.71*	**3.65**	G3	2.51	2.49	**3.44**
G9	2.53	2.44	*2.67*	G7	2.47	2.48	**3.56**
G13	2.41	2.38	**5.81**	G15	2.43	2.46	**3.04**
G21	2.45	2.50	**8.30**	G19	*2.66*	2.51	**3.02**
G2	*2.68*	*2.84*	**2.79**	G2	**3.19**	**3.23**	**3.79**
G8	2.53	2.53	*2.91*	G8	2.58	2.53	*2.81*
G14	*2.73*	*2.70*	**3.45**	G14	2.54	2.61	**3.22**
G20	**3.06**	**3.08**	**3.86**	G20	*2.66*	*2.81*	**3.32**

Table 2. SASA (nm^2) per G base ring (including exocyclic atoms) averaged over the trajectories.

	SASA (nm^2)		
	Tel22	**Tel21 Neutral**	**Tel21 Cations**
G1	0.110	0.263	0.353
G2	0.075	0.088	0.054
G3	0.077	0.061	0.172
G7	0.143	0.146	0.161
G8	0.075	0.069	0.162
G9	0.232	0.229	0.184
G13	0.119	0.234	0.114
G14	0.114	0.118	0.142
G15	0.009	0.098	0.188
G19	0.123	0.125	0.166
G20	0.167	0.146	0.120
G21	0.236	0.209	0.718

Figure captions

Fig. 1. Schematic representation of Tel21/Tel22 in antiparallel basket-type topology, based on the NMR structure (PDB ID 143D). Gs with *syn* and *anti* orientation of the glycosidic bond are depicted as orange and blue rectangular forms, respectively. The Thymine-Thymine-Adenine (TTA) residues of lateral loops (connecting adjacent antiparallel strands arranged on the same face) are shown as grey (LL1) and red (LL2) circles; the residues of the diagonal loop (DL) (connecting opposite antiparallel strands) are shown in green. The sodium ions in the channel are represented by black circles. The 5'-terminal Adenine in Tel22 (denoted as A0) is shown in light blue (dashed line plus circle).

Fig. 2. Tetrad arrangements in the Tel21 starting NMR structure for the MD simulations. Stick representation of (A) tetrad1; (B) tetrad2; (C) tetrad3. Inner and outer hydrogen bonds (between heavy atoms) are highlighted with yellow and green dashed lines, respectively. As an example, the labels for the atoms involved in h-bonds in a G pair are shown; only for G1 the labels are for all G atoms. Magenta circles are used to highlight potential deprotonation sites.

Fig. 3. Representative structure of Tel21/Tel22 simulations (closest to the average structure calculated over the trajectory). The bases of the loops are depicted in different colors: LL1 (grey), LL2 (magenta), DL (green). (A) Overall view of Tel21. Some recurrent h-bonds displayed by LL1 and LL2 bases are shown in dashed yellow lines; (B) Close-up of Tel21 DL stacking interactions (gray dashed lines) with tetrad1 bases (5'end G1 in blue, 3'end G21 in red, G9 and G13 in yellow). This DL conformation is denoted as *conformation2* in the main text; (C) Close-up of Tel22 DL stacking interactions. Tetrad1 is highlighted in yellow (G13) and light yellow (G1, G9, G21). The additional A0 base at the 5'end is shown in blue. This DL conformation is denoted as *conformation1* in the main text.

Fig. 4. Representative structures of cationic systems. (A) Cations in Tetrad1; (B) Cations in Tetrad2; (C) Cations in Tetrad3. G^+ is highlighted in purple. Tetrad1 is depicted in cyan, Tetrad2 in yellow, and Tetrad3 in light blue. The representative structure is extracted from the trajectory as the closest to the average structure (by using rmsd on all atoms).

Fig. 5. Time evolution of RMSD per-tetrad ($RMSD_{tetrad}$) in simulations of models containing G^+ in tetrad1. (A) Tel21$G1^+$; (B) Tel21$G1^+$_2; (C) Tel21$G9^+$; (D) Tel21$G9^+$_2; (E) Tel21$G13^+$; (F) Tel21$G13^+$_2; (G) Tel21$G21^+$; (H) Tel21$G21^+$_2. The RMSD is calculated on G ring atoms (including exocyclic atoms) once superimposed one tetrad at a time. The reference structure is the pdb 143D structure (model 1). Tetrad1 is shown in black, tetrad2 in red, and tetrad3 in green. The time evolution of the RMSD obtained for Tel21 is reported in the SI (**Fig. S6**).

Fig. 6. Representative structures of tetrad1 Tel21 G^+ systems. (A) Tel21$G1^+$; (B) Tel21$G9^+$; (C) Tel21$G13^+$; (D) Tel21$G21^+$. In each panel, a close-up of the tetrad1 h-bonding arrangement is shown on the left; on the right, the whole structure is schematically represented (the color code from 5'- to 3'-end is blue to red). G^+ is magenta; Na^+ ions are grey spheres. For the sake of clarity, only heavy atoms are shown. In panel D (left side) the bases of tetrad2 in yellow and tetrad3 in blue are also highlighted as transparent sticks.

Fig. 7. Interactions of N2/C8 groups with waters in Tel22 (black), Tel21 (red) and Tel21$^+$ (blue) simulations. (A) Average distance between water oxygen atoms (solvent Ow) and G N2 atoms (solute) calculated in the structures along the trajectories where at least one solute-solvent interaction is present (see the text about the criteria for the occurrence of the interaction); (B) Percentage of frames (out of 20000) which show at least one C8-Ow interaction; (C) Average distance between Ow and C8 atoms calculated in the structures along the trajectories where at least one interaction Ow-C8 is present; (D) Average number of C8-interacting water molecules per frame (fract_wat).
The blue triangles correspond to the values for each specific base in the simulations where it is charged. The values for Tel21 are derived by averaging the mean values calculated for the ten independent trajectories of Tel21 system.

Fig. 8. Schematic representation of the different factors affecting the localization of the hole and the reactivity of G^+ in quadruplexes. A single arrow connects each factor with one of the outcomes (e.g. cations affect the preferred location of G^+, mainly due to their influence on the topology and the necessity of minimizing electrostatic repulsion). A double arrow instead denotes the mutual influence between two effects (e.g. the location of G^+ is easier on regions which can be more easily distorted and, on the same time, can induce additional distortions).

Figure 1

Click here to access/download;Figure;Fig1.tif

Livello

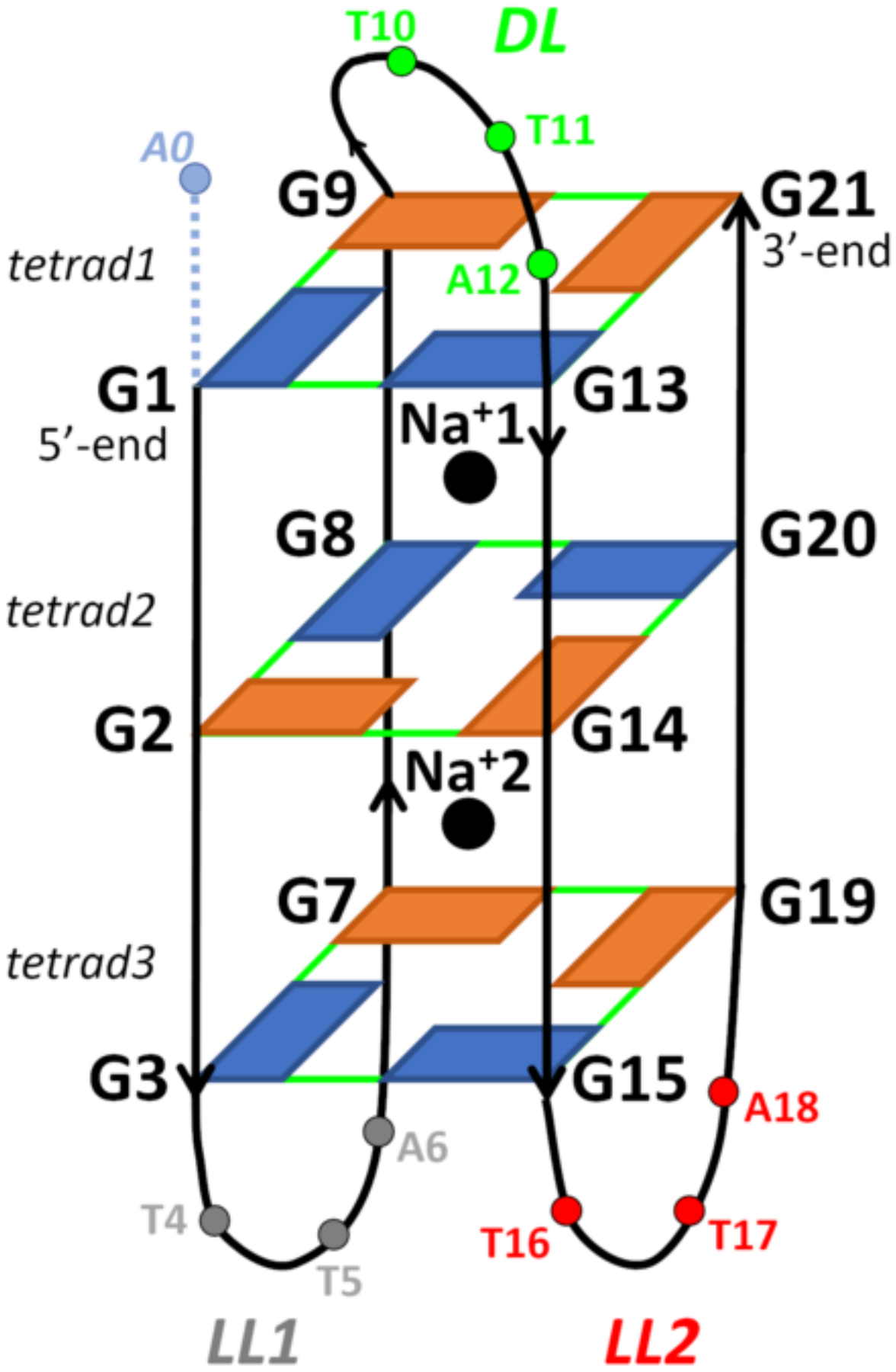

Figure 2

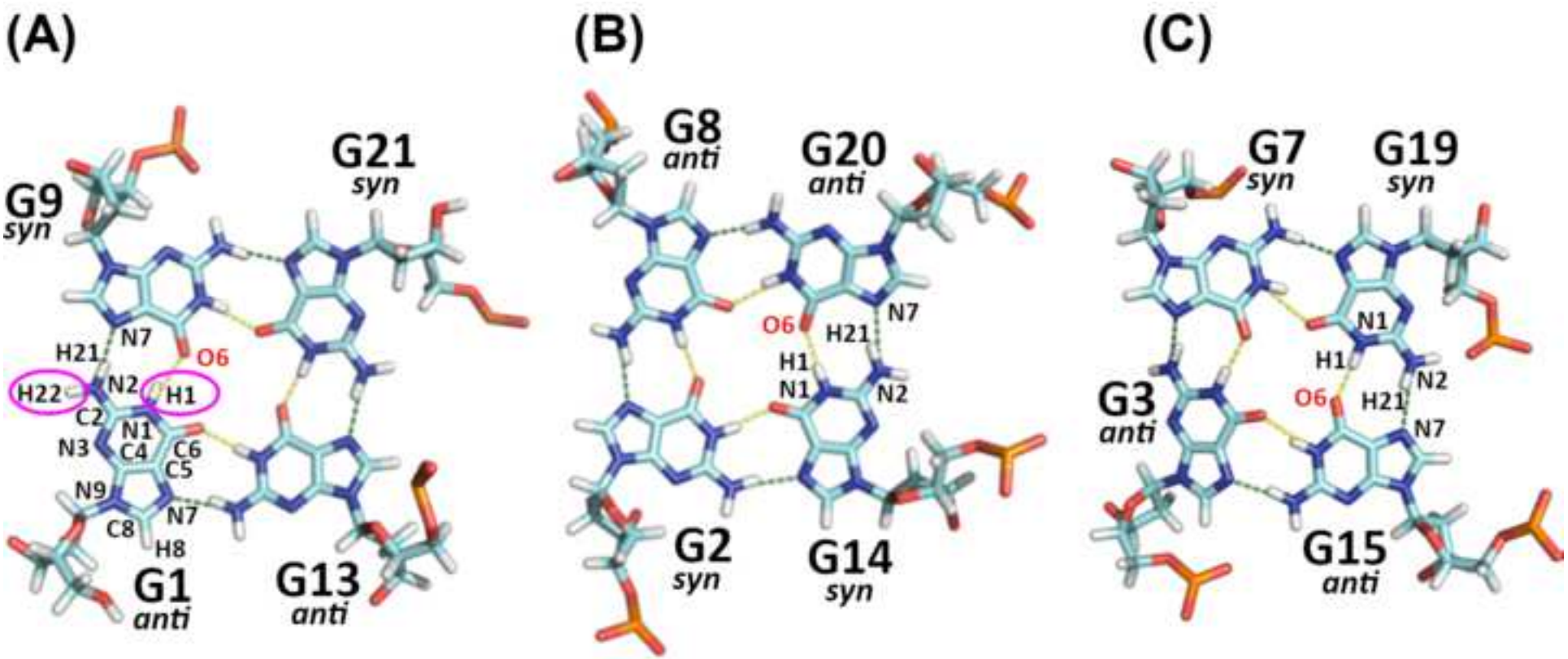

Sfondo

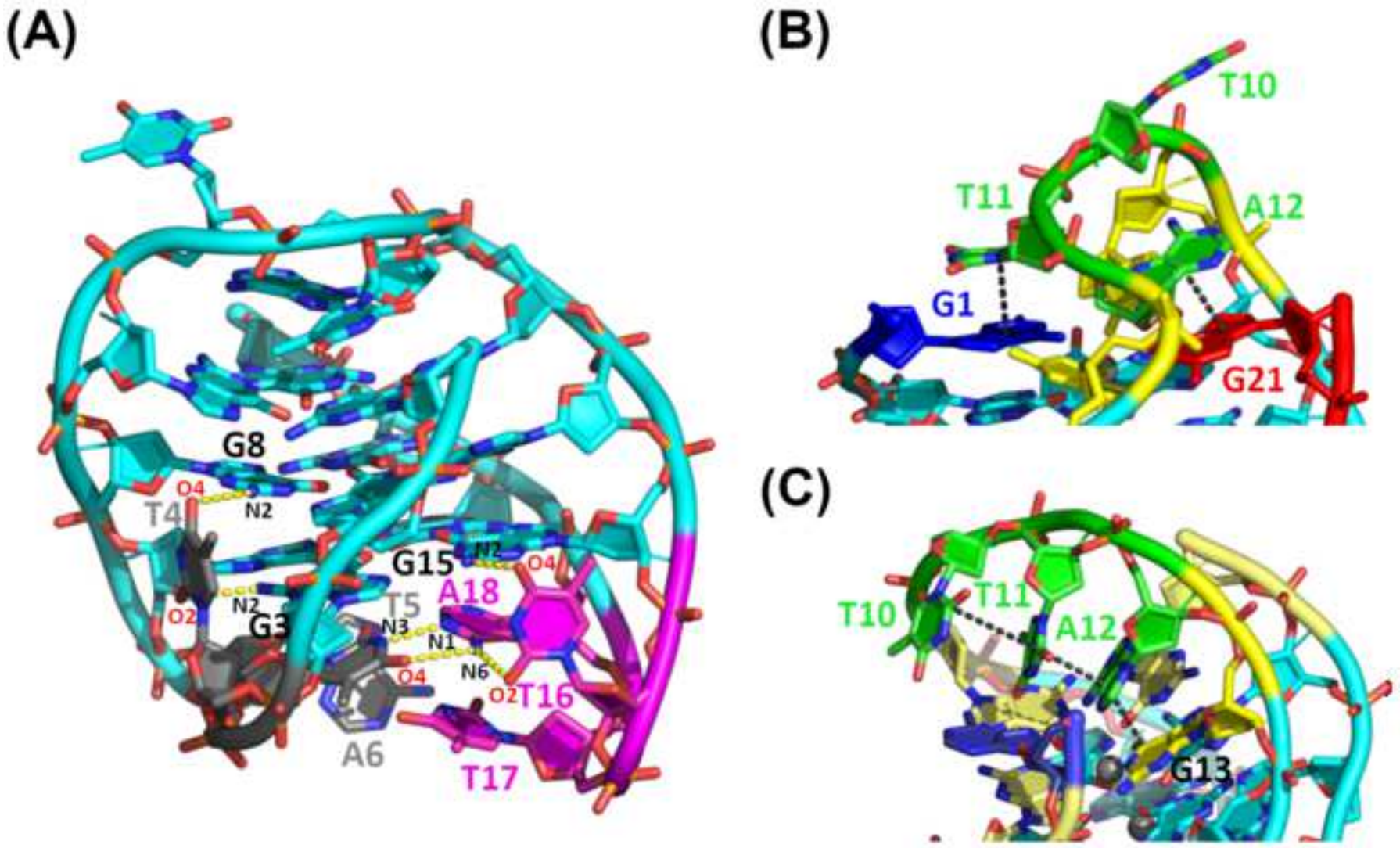

Figure 4

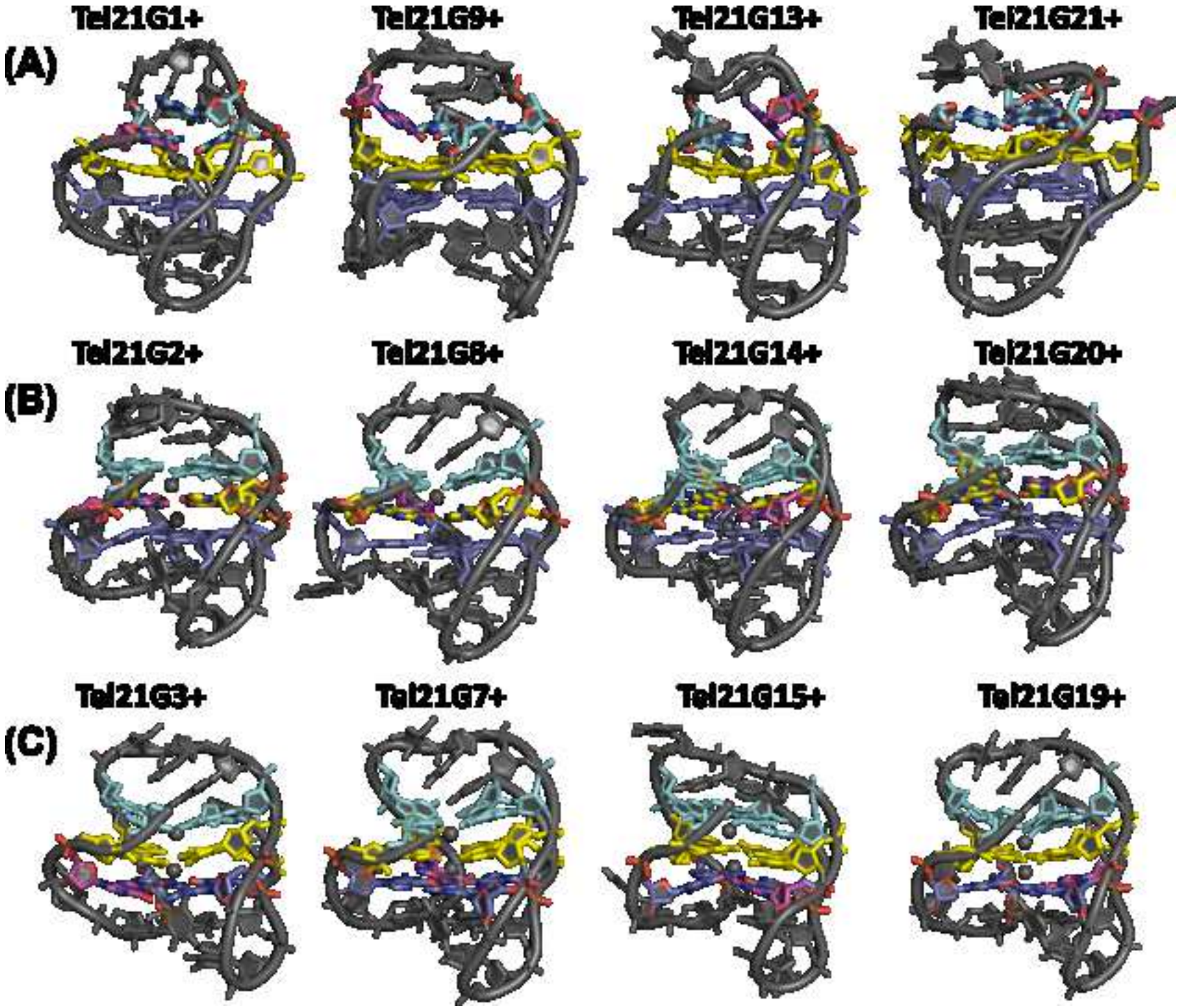

Figure 5

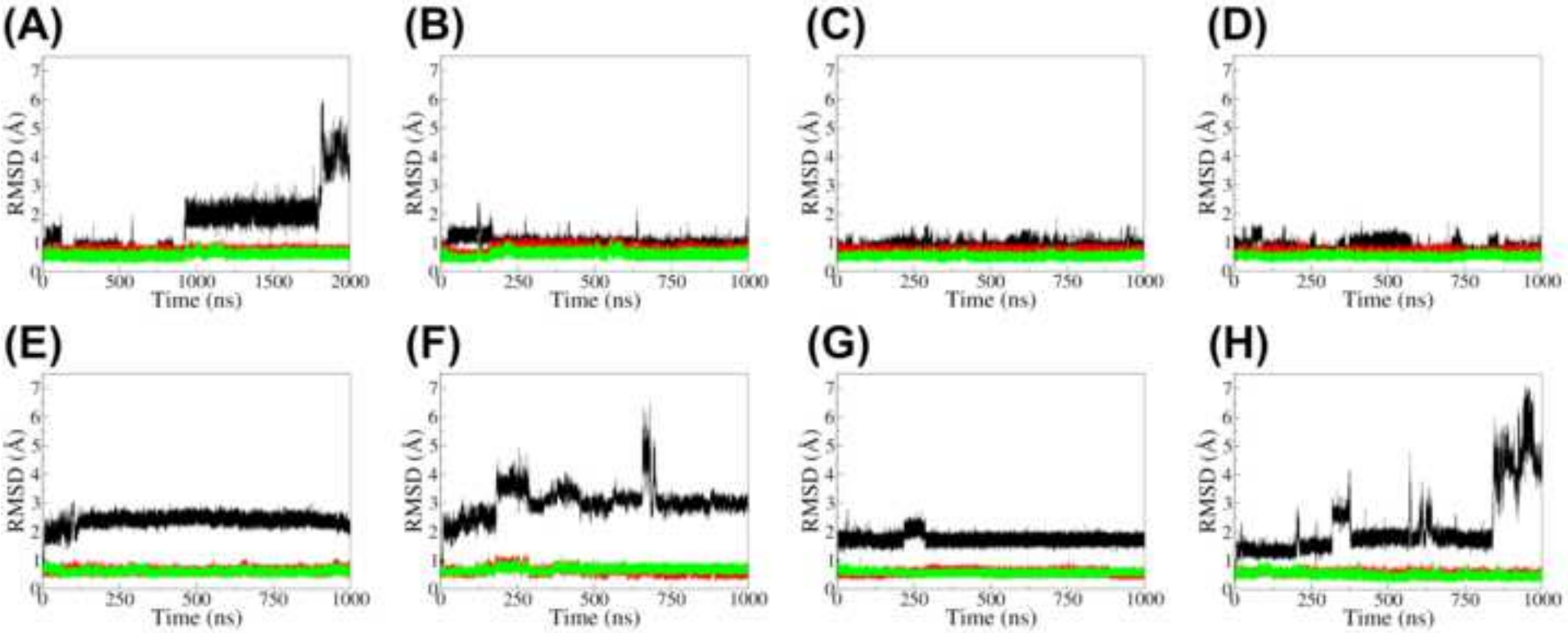

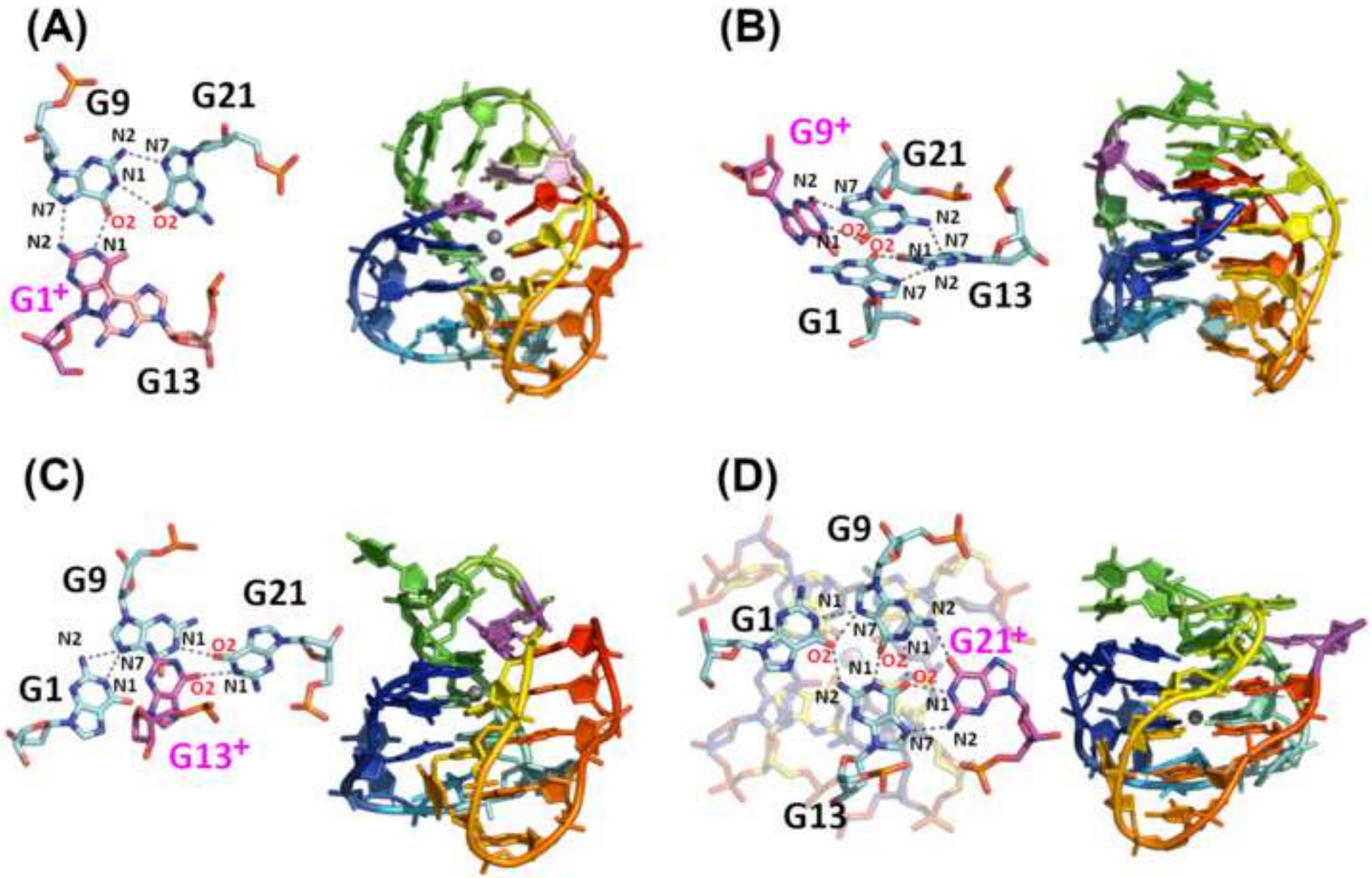

Figure 7

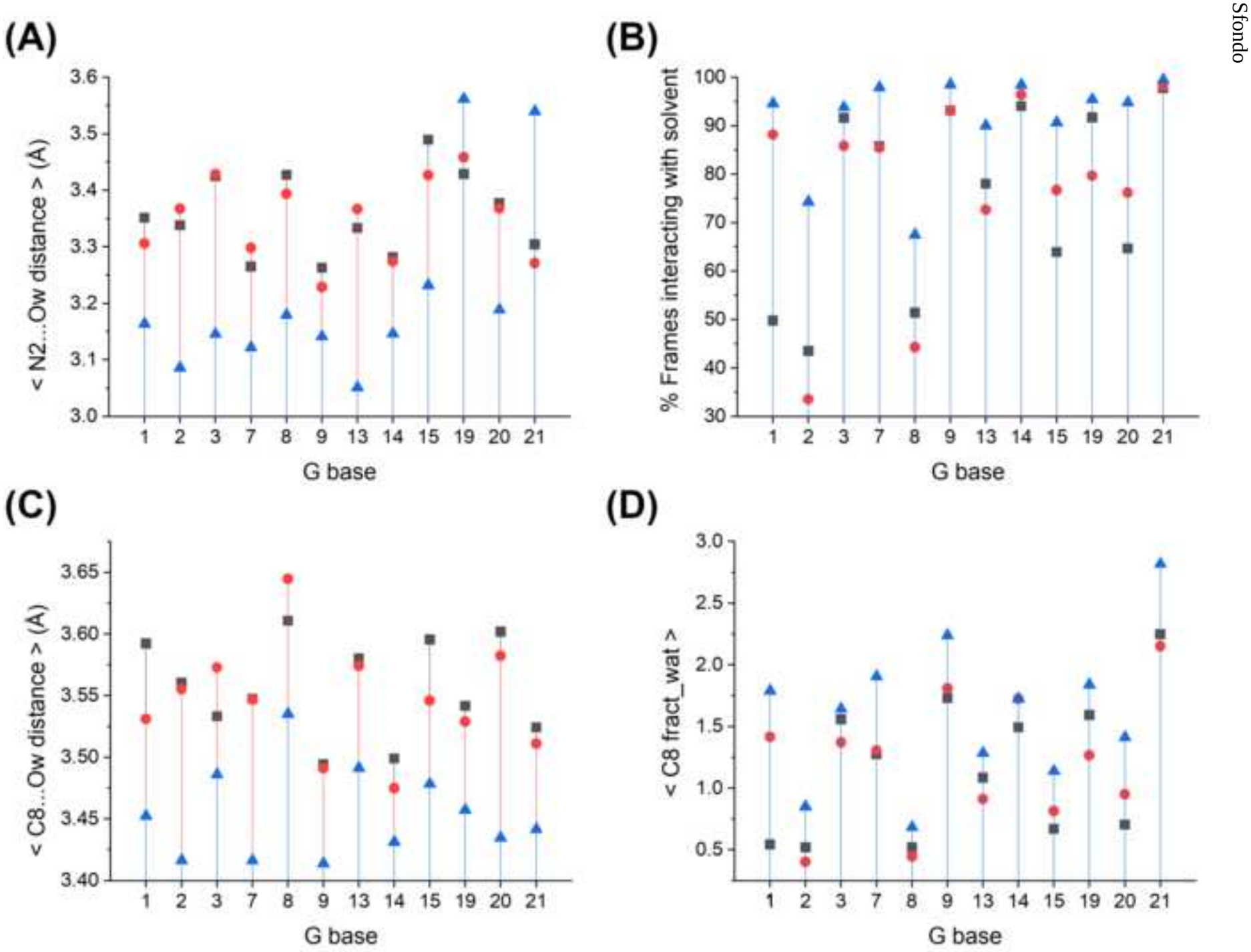

Sfondo

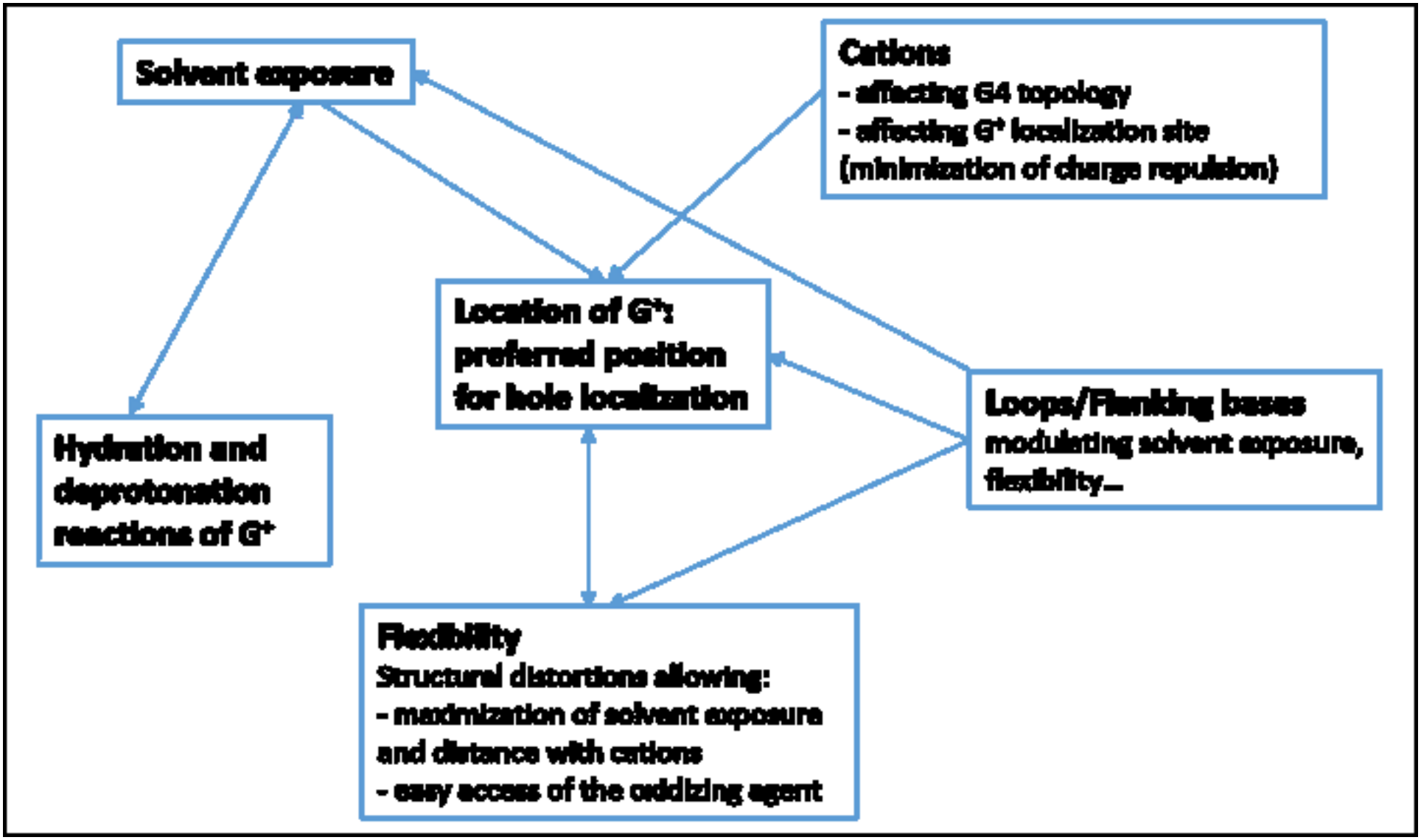

scheme8.tif

Haritha Asha: Investigation, Formal analysis, Writing

Petr Stadlbauer: *Investigation, Formal analysis, Writing*

Lara Martinez-Fernandez: Investigation, Formal analysis, Writing

Pavel Banáš: Methodology, Investigation

Jiří Šponer: Conceptualization, Methodology, Supervision, Funding acquisition, Writing

Roberto Improta: Conceptualization, Methodology, Supervision Funding acquisition Writing

Luciana Esposito: Conceptualization, Methodology, Investigation, Supervision, Writing